The Astrophysical Journal Supplement Series, 280:73 (19pp), 2025 October https://doi.org/10.3847/1538-4365/adf8ed

AllBRICQS: The Discovery of Luminous Quasars in the Northern Hemisphere

Yunyi Choi[1], Yuming Fu[2,3], Myungshin Im[1], Xue-Bing Wu[4,5], Christopher A. Onken[6,7], Christian Wolf[6,7], Seo-Won Chang[1], Hyeonho Choi[1], Mankeun Jeong[1], Yongjung Kim[8], Gu Lim[9,10], Yuxuan Pang[4,5], Taewan Kim[1], Jubee Sohn[1], Dohyeong Kim[9], Ji Hoon Kim[1], Eunhee Ko[1], Gregory S. H. Paek[11], and Sungho Jung[1]

[1] SNU Astronomy Research Center, Department of Physics & Astronomy, Seoul National University, 1 Gwanak-ro, Gwanak-gu, Seoul 08826, Republic of Korea; myungshin.im@gmail.com
[2] Leiden Observatory, Leiden University, Einsteinweg 55, 2333 CC Leiden, The Netherlands
[3] Kapteyn Astronomical Institute, University of Groningen, P.O. Box 800, 9700 AV Groningen, The Netherlands
[4] Department of Astronomy, School of Physics, Peking University, Beijing 100871, People's Republic of China
[5] Kavli Institute for Astronomy and Astrophysics, Peking University, Beijing 100871, People's Republic of China
[6] Research School of Astronomy and Astrophysics, Australian National University, Cotter Road, Weston Creek, ACT 2611, Australia
[7] Centre for Gravitational Astrophysics, Australian National University, Building 38 Science Road, Acton, ACT 2601, Australia
[8] School of Liberal Studies, Sejong University, 209 Neungdong-ro, Gwangjin-Gu, Seoul 05006, Republic of Korea
[9] Department of Earth Sciences, Pusan National University, Busan 46241, Republic of Korea
[10] Institute for Future Earth (IFE), Pusan National University, Busan 46241, Republic of Korea
[11] Institute for Astronomy, University of Hawaii, 2680 Woodlawn Drive, Honolulu, HI 96822, USA
Received 2025 June 12; revised 2025 July 21; accepted 2025 August 5; published 2025 October 9

Abstract

We present the second catalog of bright quasars from the All-sky BRIght, Complete Quasar Survey (AllBRICQS), focusing on spectroscopically observed quasars in the Northern Hemisphere with Galactic latitude $|b| > 10°$. This catalog includes their spectral data, redshifts, and luminosities. AllBRICQS aims to identify the last remaining optically bright quasars using data from the Wide-field Infrared Survey Explorer and Gaia all-sky survey Data Release 3 (DR3). AllBRICQS searches for quasars that are brighter than $B_P = 16.5$ or $R_P = 16$ mag in Gaia DR3, based on simple selection criteria. Here, we report 62 new AllBRICQS quasars spanning various types, which include typical broad emission line quasars and the most luminous iron low-ionization broad absorption line quasars discovered to date. Spectroscopic observations were conducted using the Long-Slit Spectrograph on the 1.8 m telescope at Bohyunsan Optical Astronomy Observatory, the Yunnan Faint Object Spectrograph and Camera on the 2.4 m telescope at Lijiang Observatory, and the Beijing Faint Object Spectrograph and Camera on the 2.16 m telescope at Xinglong Observatory. We applied flux calibration using Zwicky Transient Facility broadband photometry to correct for attenuation due to intermittent thin clouds during the observations. Redshifts were determined using inverse-variance weighted cross-correlation methods. Our targets span the bolometric luminosity range of $44.9 < \log(L_{\rm bol}/{\rm erg\ s^{-1}}) < 48.0$ at redshifts between 0.09 and 2.48. These confirmed AllBRICQS quasars provide a valuable resource for future research into quasar evolution, black holes, their environments, and their host galaxies across multiple wavelengths.

Unified Astronomy Thesaurus concepts: Quasars (1319); Active galactic nuclei (16); Spectroscopy (1558); Redshift surveys (1378); Catalogs (205)

Materials only available in the online version of record: figure set, machine-readable table

1. Introduction

A quasar is an active galactic nucleus (AGN) with a bolometric luminosity of $L_{\rm bol} \geqslant 10^{45}$ erg s^{-1}. Powered by a central black hole (BH), a quasar interacts with its host galaxy and influences the surrounding circumgalactic medium through energetic outflows. When a quasar is optically bright, its high-signal-to-noise ratio (SNR) facilitates detailed investigations into its physical mechanisms and interactions with the environment.

From more common, modestly growing BHs to rare, rapidly growing BHs at greater distances, bright quasars provide valuable insights into the mass and Eddington ratio of their central BHs. Since a brighter quasar flux is associated with a larger broad-line region (BLR; M. C. Bentz et al. 2013), direct high spatial resolution investigation can enable direct imaging of the BLR, allowing precise measurement of its size (GRAVITY Collaboration et al. 2018, 2020, 2021a, 2021b). The inherent brightness of these quasars makes them ideal targets for continuous time-series observations, facilitating variability studies that deepen our understanding of accretion disk processes in AGNs (Z. Li et al. 2018; P. Sánchez-Sáez et al. 2018).

Because of their importance, bright quasars ($V \lesssim 17$ mag) have been searched extensively, dating back to as early as 1983 (M. Schmidt & R. F. Green 1983; H. J. Hagen et al. 1995; P. C. Hewett et al. 1995; R. H. Becker et al. 2001; D. P. Schneider et al. 2005; M. Im et al. 2007; I. Lee et al. 2008; J. Yang et al. 2023; Y. Kim et al. 2024c; S. J. Nakoneczny et al. 2025). Despite these efforts, there seems to be a substantial number of bright quasars that have been missed in previous surveys. Recent discoveries of new bright quasars demonstrate that previous studies have missed such objects (I. Lee et al. 2008; C. A. Onken et al. 2022; C. Wolf et al. 2024). The reasons for these missed detections may include low survey completeness, incomplete selection criteria, and photometric flag issues, although it remains difficult to verify conclusively. Additionally, a large number of low Galactic latitude quasars have been found recently (M. Im et al. 2007; Y. Fu et al. 2022; J. Werk et al. 2024; Z.-Y. Huo et al. 2025).

More recently, the low-resolution prism spectra from the Gaia mission have been used to construct a comprehensive quasar candidate catalog, Quaia (K. Storey-Fisher et al. 2024). However, this catalog may fail to identify some bright quasars, and the redshift estimates can be imprecise due to the limited spectral resolution (see Section 6.1 for details). To accurately characterize quasars and derive key physical properties such as BH mass, higher-resolution spectroscopic observations are essential.

To address the need for identifying the remaining optically bright quasars, the All-sky BRIght, Complete Quasar Survey (AllBRICQS) project (C. A. Onken et al. 2023) was initiated as an ongoing effort to discover previously undetected bright quasars using all-sky data: Gaia Data Release 3 (DR3; Gaia Collaboration et al. 2016, 2021) and the Wide-field Infrared Survey Explorer (WISE; E. L. Wright et al. 2010; A. Mainzer et al. 2014). The first publication in this series, C. A. Onken et al. (2023), reported 156 spectroscopically confirmed quasars discovered using the Wide Field Spectrograph (WiFeS; M. Dopita et al. 2007, 2010) on the Australian National University (ANU) 2.3 m telescope at Siding Spring Observatory (SSO). This selection method, based on four straightforward criteria (detailed in Section 2), demonstrated high efficiency in identifying bright quasars. Following on this effort, we have conducted spectroscopic observations of ALLBRICS quasar candidates in the Northern Hemisphere.

This paper presents the results from the spectroscopic observations of AllBRICQS quasar candidates in the Northern Hemisphere. Section 2 outlines the quasar candidate selection criteria established in the previous AllBRICQS paper (C. A. Onken et al. 2023), discussing the purity and completeness of this selection method. Section 3 describes the observations carried out using telescopes at three different observatories. Section 4 details the spectral data reduction process, including flux scaling, target classification, redshift estimation, and bolometric luminosity measurements. Section 5 presents the classification results of the AllBRICQS sample, discusses their properties, and highlights quasars with distinctive spectral features. Section 6 provides a comparison between our newly discovered quasars and those from other surveys. Finally, Section 7 summarizes the main findings of this study.

We adopt a flat ΛCDM cosmology with a matter density of $\Omega_{\rm m} = 0.3$ and a Hubble–Lemaître constant of $H_0 = 70\,{\rm km\,s^{-1}\,Mpc^{-1}}$. Throughout this paper, all magnitudes are given in the Vega system unless otherwise specified.

2. Candidate Selection

AllBRICQS (C. A. Onken et al. 2023) identifies quasar candidates more effectively than previous methods by utilizing data from the WISE catalog (E. L. Wright et al. 2010; A. Mainzer et al. 2014) and precise parallax and proper-motion (PPM) measurements from Gaia DR3. The AllBRICQS selection method focuses on quasar candidates with $B_P < 16.5$ or $R_P < 16.0$ mag, a range where stars, galaxies, and quasars can be more reliably distinguished. The selection criteria, thoroughly detailed in C. A. Onken et al. (2023), consist of four key requirements:

1. Galactic latitude $|b| > 10°$: reduces contamination from the Galactic plane, where stellar density is high.
2. Gaia PPM $< 4\sigma$: ensures the selection of extragalactic sources by filtering out objects with significant measurable motion, typical of stars within the Milky Way.
3. B_P/R_P excess factor < 1.5 (point source):[12] Differentiates between resolved (galaxies) and unresolved (stars and quasars) sources. It refers to `phot_bp_rp_excess_factor` (C; D. W. Evans et al. 2018; M. Riello et al. 2021).
4. WISE W1 − W2 > 0.2 mag: Utilizes mid-infrared color selection to distinguish AGNs from stars and low-redshift galaxies. Profile-fit magnitudes from the AllWISE catalog[13] are used.

Although the original AllBRICQS selection process inadvertently used AllWISE magnitudes, it was intended to rely on CatWISE photometry (P. R. M. Eisenhardt et al. 2020; F. Marocco et al. 2021), which offers improved source deblending and astrometric precision. In this work, we present all W1 − W2 color values using CatWISE magnitudes when available, and supplement with AllWISE when necessary. This correction affects only a small number of sources near the W1 − W2 = 0.2 threshold and has minimal impact on the overall sample distribution.

By applying these criteria, the first AllBRICQS paper (C. A. Onken et al. 2023) identified 290 quasar candidates. Among them, 166 were observed using the ANU 2.3 m telescope at SSO with the WiFeS instrument (M. Dopita et al. 2007, 2010). Spectroscopic confirmation was achieved for 156 candidates, including 140 newly discovered quasars. Based on these results, C. A. Onken et al. (2023) estimated the selection purity of the AllBRICQS method to be approximately 96%. Many of the remaining unobserved candidates have since been followed up at facilities in the Northern Hemisphere.

To evaluate the completeness of our selection method, C. A. Onken et al. (2023) tested it against the Million Quasars Catalogue v7.2 (Milliquas; E. W. Flesch 2021) using Gaia sources with $B_P < 17$ mag, redshifts $z > 0.3$, and Galactic latitudes $|b| > 10°$. The completeness is approximately 96.5%, demonstrating the robustness of our criteria. While a few quasars were excluded due to the absence of PPM measurements, the vast majority were consistent with being drawn from the statistical tails of a zero-PPM population. This underscores the stringent nature of the AllBRICQS selection, which was designed to maintain both high purity and completeness.

3. Observations

To expand the AllBRICQS sample and investigate bright quasar candidates in the Northern Hemisphere, we conducted long-slit spectroscopic observations of 75 targets from the 82 remaining candidates yet to be observed in this region. As illustrated in Figure 1, these candidates are not confined to previously unexplored regions; they also include objects

[12] This selection may exclude AGNs with significant host galaxy contributions detectable by Gaia DR3, thereby introducing a bias against AGNs or quasars at $z < 0.3$, as well as against lensed quasars with resolved lens galaxies or blended lensed images.

[13] https://wise2.ipac.caltech.edu/docs/release/allwise/expsup/index.html

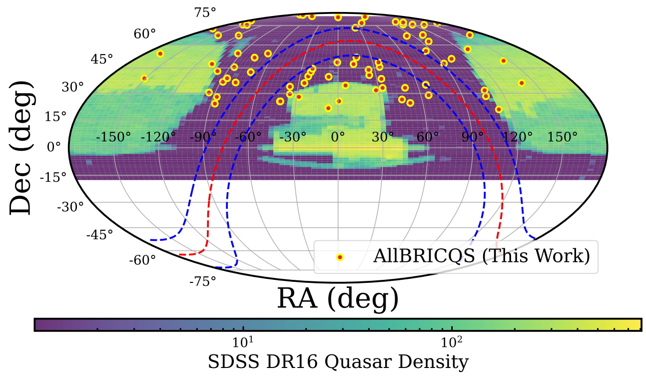

Figure 1. The sky positions of the 75 observed targets are overplotted on the SDSS footprint. Red points with yellow outlines indicate the observed sources. The red and blue dashed lines represent Galactic latitudes of $b = 0°$ and $b = \pm 10°$, respectively.

located within the footprint of the Sloan Digital Sky Survey Data Release 16 Quasar Catalog (SDSS DR16Q; R. Ahumada et al. 2020), as discussed in detail in Section 6.2.

Among the 75 targets, 68 were observed with the 1.8 m telescope at the Bohyunsan Optical Astronomy Observatory (BOAO) in South Korea. An additional eight and four targets were observed with the Lijiang 2.4 m telescope (LJT) at the Lijiang Observatory (LJO; C.-J. Wang et al. 2019) and the Xinglong 2.16 m telescope (XLT) at the Xinglong Observatory (XLO; Z. Fan et al. 2016), respectively, both located in China. Notably, five candidates were observed at multiple observatories to ensure consistency and data quality. The observations were conducted between UT 2022 October 27 and 2024 December 1.

BOAO is located at 36°09′52.8″N, 128°58′35.8″E in South Korea. Observations at BOAO utilized the Long-Slit Spectrograph, configured with a slit width of 3″.6 and covering a wavelength range from 3500 to 10500 Å. The 150 V grating provided a dispersion of 5.2 Å pix^{-1}, and a spectral resolution of $R \sim 280$. This spectroscopic setup closely resembles that used in the SNUQSO bright quasar survey conducted at BOAO with the same instrument (M. Im et al. 2007; I. Lee et al. 2008). Spectra were obtained over six nights between UT 2022 October 27 and 2024 December 1, covering a broad wavelength range essential for redshift determination and luminosity measurements.

The LJO is located at 26°41′42″N, 100°01′48″E, while the XLO is situated at 40°23′39″N, 117°34′30″E, both in China. At LJO, we used the Yunnan Faint Object Spectrograph and Camera (YFOSC), configured with slit widths of 1″.8 and 2″.5, covering a wavelength range of 5120–9850 Å. The grism provided a dispersion of 1.5 Å pix^{-1}, corresponding to a spectral resolution of $R \sim 600$ and 800 at 6600 Å, depending on the slit width. These spectra were acquired over four nights between UT 2022 December 13 and 2023 February 24, contributing valuable data to the AllBRICQS sample.

At XLO, we employed the Beijing Faint Object Spectrograph and Camera (BFOSC; Y. Zhao et al. 2018), which covers a wavelength range of 4107–6724 Å with a slit width of 2″.3 and a dispersion of 1.34 Å pix^{-1}, corresponding to $R \sim 550$ at 5100 Å. The spectra at XLO were obtained over a single night on UT 2022 November 12.

To ensure accurate spectral calibration, we observed various spectrophotometric standard stars alongside the AllBRICQS candidates. These standard stars were used to calibrate the overall spectral shape. However, since the standard stars were not necessarily observed under identical conditions, we also applied photometry data for absolute flux calibration. Instead, flux scaling was addressed separately, as detailed in Section 4.2.

4. Data Calibration

4.1. Data Reduction

For BOAO observational data, we employed the Image Reduction and Analysis Facility (IRAF; D. Tody 1986, 1993) for standard reduction procedures, including bias subtraction and flat-field correction. Cosmic-ray removal was performed using `astroscrappy`, an optimized implementation of the P. G. van Dokkum (2001) algorithm within the `astropy` framework (C. McCully et al. 2018).

Wavelength calibration for the BOAO data was performed by matching observed emission lines to a reference spectrum from a FeNeArHe arc lamp. This lamp provides a wide range of well-defined emission lines, enabling accurate calibration across the full spectral range. The resulting wavelength calibration error was consistently smaller than the spectral dispersion of 5.2 Å pix^{-1}, confirming the reliability of the calibration procedure. In addition, heliocentric velocity corrections were applied based on the location and timing of each observation to account for Earth's motion relative to the observed targets.

For initial flux calibration, we utilized spectrophotometric standard stars observed on the same night, at similar airmass, and within an intermediate time frame relative to the science targets. The reference spectra of the standard stars were derived from theoretical models and observational data from STIS, MMT, and ESO (M. Hamuy et al. 1992, 1994; R. C. Bohlin et al. 2014, 2020).

The reliable wavelength range of each spectrum varied slightly depending on the observation date. Notably, data from UT 2022 October 27 exhibited a problem with focus at longer wavelengths, leading to unreliable flux measurements (SNR < 5) at $\lambda \gtrsim 7600$ Å. Despite this anomaly, spectra from the other BOAO observing dates provide reliable flux measurements over the 4000–9000 Å range. These calibrated and reduced spectra serve as the foundation for further analysis, including redshift and bolometric luminosity estimations detailed in the following sections.

The spectroscopic data from the LJT/YFOSC and XLT/BFOSC were reduced using a Python package `pyfosc` (Y. Fu & Y. Li 2024), which follows the standard procedures of IRAF (D. Tody 1986, 1993) for spectroscopic data reduction. The cosmic-ray removal was also conducted with `astroscrappy` (P. G. van Dokkum 2001; C. McCully et al. 2018). A FeAr arc lamp was used for wavelength calibration of the XLT/BFOSC data, while a HeNeAr arc lamp was used for the LJT/YFOSC data. The reliable wavelength range of each spectrum is 5100–9300 Å for the LJT/YFOSC data and 4100–6700 Å for the XLT/BFOSC data.

4.2. Flux Scaling

Accurate flux scaling is essential to ensure that spectroscopic data reflect the real-time flux levels of quasar targets. Due to intermittent thin cloud coverage during our observing run, some target fluxes were attenuated. To correct for this, we applied an additional flux-scaling step using light curve data from the Zwicky Transient Facility Data Release 22 (ZTF

DR22; E. C. Bellm et al. 2019; F. J. Masci et al. 2019), following the initial spectrophotometric calibration with standard stars. The flux-scaling process utilizes *r*-filter photometry acquired on the exact date of our spectroscopic observations, providing a robust match to the spectral data and mitigating the effects of both atmospheric transparency variations and intrinsic quasar variability.

For the XLT data, where the spectral coverage does not fully overlap with the *r*-filter transmission range, we used *g*-filter photometry instead. If photometric data were unavailable for the observation date, we employed linear interpolation of the ZTF light curve to estimate the expected magnitude. For data collected on UT 2024 December 1, since the ZTF DR22 data set includes observations only up to UT 2024 July 1, we flux scaled the spectra using the most recent available photometric data to minimize the impact of temporal discrepancies. The synthetic photometry results for the ZTF *g*- and *r*-filters of the quasars are presented in Appendix A.

4.3. Target Classification and Redshift Measurement

Spectral classification and redshift estimation were initially conducted through visual inspection of the observed spectra. In cases where classification was ambiguous, the MARZ online application was used to assist the identification process (S. Hinton 2016; S. R. Hinton et al. 2016).

Final redshift values (heliocentric redshifts) and their associated uncertainties were derived using `RVSNUpy` (T. Kim et al. 2025), a Python-based tool that estimates redshifts by performing inverse-variance weighted cross correlation between the observed spectra and a library of rest-frame template spectra. Approximately 79% of the quasar sample exhibits redshift uncertainties (δz) smaller than 0.0005, while 92% have $\delta z < 0.001$. For a small number of quasars, redshift values and redshift uncertainties could not be determined due to either blended emission and absorption features or low SNR in regions containing key spectral lines.

In Table 1, the redshift measurements are reported in the "AllBRICQS" column under the "Redshift" header. For targets whose redshifts could not be determined using `RVSNUpy`, approximate values with reduced significant figures and large uncertainties are listed. Note that additional redshift uncertainty, up to 0.004, may arise from the wavelength calibration process. This calibration-related uncertainty is not included in the redshift errors presented in the table.

4.4. Bolometric Luminosity

The bolometric luminosity is a critical parameter for characterizing quasars, providing insights into the energy output of the accretion process around BHs. We calculated the bolometric luminosity for each flux-scaled quasar spectrum, applying robust extinction corrections to ensure accurate luminosity estimates.

We used `PyQSOFit` (H. Guo et al. 2018; Y. Shen et al. 2019) to derive continuum luminosities. For Galactic extinction correction, we applied the default settings: the dust map from D. J. Schlegel et al. (1998), a standard Milky Way reddening parameter of $R_V = 3.1$, and the extinction model from E. L. Fitzpatrick (1999). The continuum fitting was performed over the 4000–9000 Å range, using spectral regions selected to be relatively free of strong emission lines. The continuum model consists of a power-law component combined with a third-order polynomial to account for broad spectral curvature. Bolometric luminosities were then estimated using the method outlined in J. C. Runnoe et al. (2012a, 2012b), which provides empirically calibrated bolometric corrections at rest-frame wavelengths of 1450, 3000, and 5100 Å. When multiple continuum luminosities were available, we adopted the mean value (see Table 5 of Appendix B).

To account for host galaxy dust extinction, we performed spectral energy distribution fitting using photometric magnitudes from SDSS, Pan-STARRS, Two Micron All Sky Survey, and WISE, incorporating a reddening law from E. L. Fitzpatrick (1999) and following the method described in D. Kim et al. (2023). We calculated the AGN continuum luminosities at 3.4 and 4.6 μm, and then derived the bolometric luminosities based on the relations presented by D. Kim et al. (2023, 2024a, 2024b), applying extinction corrections. The resulting bolometric luminosities from the extinction-corrected infrared continuum are in reasonable agreement with those estimated from the rest-frame ultraviolet and optical continuum luminosities at 1450, 3000, and 5100 Å. This agreement suggests that our sample does not include any heavily dust-obscured quasars.

Figure 2 displays the measured redshift and log bolometric luminosity values of AllBRICQS quasars. These quasars predominantly occupy the bright end of the quasar distribution, represented by the gray contours of SDSS DR16 quasars (B. W. Lyke et al. 2020). Note that J0633+6225 and J1809+2758, observed with XLT and LJT, respectively, are excluded from the figure. Their exclusion is due to insufficient wavelength coverage, which is essential for accurate bolometric luminosity estimation. The redshifts of these two targets are 0.33 and 2.41, respectively.

5. AllBRICQS Samples

This section presents the classification results of the 75 observed spectra, including confirmed quasars, unclassified sources, and stars. The properties of the observed targets are summarized in Figure 3. A complete list and spectral gallery of confirmed quasars are provided in Table 1 and Appendix C.1, ordered by increasing R.A. and redshift, respectively. Similarly, the unclassified sources and stars are listed in Tables 2 and 3, with their corresponding spectral galleries shown in Appendices C.2 and C.3, respectively.

The targets were divided into two priority classes based on their WISE color. Priority 1 targets are defined as sources with W1 − W2 > 0.3 mag, based on AllWISE profile-fit magnitudes. Priority 2 targets have W1 − W2 ⩽ 0.3 mag and lie closer to the stellar locus in color space. The selection purity of the Priority 1 sample is 98.4%. Notably, all stellar contaminants in our sample—except for one—were initially classified as Priority 2 targets.

5.1. Confirmed Quasars

Among the 75 observed candidates, 62 sources have been confirmed as quasars through spectroscopic analysis. The newly discovered quasars exhibit log bolometric luminosities ranging from $\log L_{\rm bol} \sim 44.9$ to $48.0\,{\rm erg\,s^{-1}}$ and redshifts spanning from 0.09 to 2.48. When we crossmatched them to the quasars in the Milliquas v8 catalog (E. W. Flesch 2023), 19 of them were identified as quasar candidates based on optical to mid-infrared photometry (A. R. Klemola et al. 1994;

Table 1
AllBRICQS Confirmed Quasars

Target	R.A. (J2000) (deg)	Decl. (J2000) (deg)	B_P (mag)	R_P (mag)	$W12$ (mag)	μ (mas yr^{-1})	Redshift AllBRICQS	Quaia	CatNorth	Others
J0002+2529	0.6584	25.4906	16.22	15.20	1.14	0.04 ± 0.05	0.3637 ± 0.0002	0.365	0.435	0.37[a]
J0052+4721*	13.1842	47.3663	16.89	15.98	1.11	0.03 ± 0.07	1.5267 ± 0.0006	⋯	⋯	⋯
J0105+5137	16.4816	51.6293	16.63	15.86	1.25	0.06 ± 0.06	0.7692 ± 0.0002	0.539	0.790	⋯
J0139+4036	24.7536	40.6120	16.23	15.57	0.73	0.02 ± 0.07	2.4860 ± 0.0008	1.154	2.209	⋯
J0141+7307	25.3294	73.1285	17.29	15.83	1.19	0.04 ± 0.06	1.5869 ± 0.0007	⋯	1.698	⋯
J0152+3143	28.0699	31.7171	16.59	16.00	1.47	0.19 ± 0.09	1.2164 ± 0.0006	⋯	⋯	1.20[b]
J0212+3306	33.2025	33.1120	16.63	15.95	1.04	0.11 ± 0.10	0.1874 ± 0.0001	0.199	0.186	⋯
J0214+3824	33.6604	38.4148	16.55	15.95	1.39	0.13 ± 0.10	1.5698 ± 0.0011	1.567	1.557	1.57[a]
J0245+7718	41.3216	77.3059	17.25	15.92	0.99	0.15 ± 0.08	1.9793 ± 0.0011	⋯	2.027	⋯
J0303+2629	45.7550	26.4884	16.80	15.95	1.25	0.04 ± 0.10	0.9068 ± 0.0001	0.654	0.916	0.91[a]
J0324+2432	51.1758	24.5459	16.20	15.30	1.04	0.09 ± 0.08	0.2472 ± 0.0001	0.245	0.473	⋯
J0503+8351	75.7822	83.8612	16.56	15.72	1.04	0.12 ± 0.06	0.2590 ± 0.0001	0.274	0.299	⋯
J0528+6633	82.1957	66.5598	16.57	15.81	0.95	0.03 ± 0.04	0.6793 ± 0.0002	0.647	1.076	⋯
J0602+4743	90.5840	47.7324	16.70	15.87	1.07	0.06 ± 0.07	0.2316 ± 0.0001	0.230	0.307	⋯
J0633+6225	98.2560	62.4288	16.27	15.57	1.07	0.02 ± 0.05	0.3343 ± 0.0001	0.335	0.341	⋯
J0643+5044	100.9192	50.7418	15.82	15.01	1.03	0.09 ± 0.05	0.2093 ± 0.0001	⋯	0.230	⋯
J0653+6716	103.3123	67.2795	16.14	15.37	1.00	0.03 ± 0.05	0.2925 ± 0.0002	0.293	0.318	⋯
J0707+2821	106.9702	28.3518	16.04	15.40	1.01	0.09 ± 0.07	1.9091 ± 0.0007	1.891	1.885	⋯
J0708+7555	107.0917	75.9217	16.38	15.76	1.30	0.02 ± 0.05	1.8851 ± 0.0012	1.883	1.864	⋯
J0708+7822	107.0212	78.3713	15.85	15.21	0.85	0.06 ± 0.04	0.2512 ± 0.0001	0.400	0.501	⋯
J0728+2056	112.1122	20.9385	16.86	15.88	0.91	0.08 ± 0.08	1.3473 ± 0.0017	⋯	2.569	⋯
J0750+7751	117.7125	77.8504	16.11	15.70	1.17	0.05 ± 0.05	0.7693 ± 0.0003	0.703	0.751	0.77[a]
J0807+7550	121.8778	75.8388	15.66	14.82	1.18	0.02 ± 0.03	0.5753 ± 0.0002	0.402	0.847	0.57[a]
J0827+5703	126.9324	57.0606	17.20	15.85	1.16	0.08 ± 0.07	1.55 ± 0.01	⋯	1.690	⋯
J0919+3557	139.9281	35.9514	16.78	15.59	0.98	0.03 ± 0.08	2.365 ± 0.001	⋯	⋯	3.30[b]
J0919+7539	139.9001	75.6623	16.38	15.89	1.16	0.06 ± 0.06	0.5238 ± 0.0002	0.517	0.537	0.52[a]
J0938+4927*	144.7180	49.4584	16.38	15.91	1.20	0.12 ± 0.06	0.7370 ± 0.0002	0.514	⋯	⋯
J1143+7727	175.8681	77.4592	16.56	16.00	1.33	0.13 ± 0.08	0.9969 ± 0.0001	0.966	1.068	⋯[c]
J1203+7226	180.7783	72.4370	16.15	15.31	0.95	0.10 ± 0.06	0.1033 ± 0.0001	0.226	0.177	⋯
J1216+7948	184.1664	79.8003	16.73	15.94	1.45	0.00 ± 0.07	1.6834 ± 0.0011	1.697	1.685	⋯
J1256+5404	194.1117	54.0742	16.54	16.00	0.97	0.05 ± 0.06	0.1993 ± 0.0001	0.279	0.280	⋯
J1317+8637	199.3724	86.6268	16.95	15.92	1.06	0.08 ± 0.06	0.2414 ± 0.0001	0.240	0.530	⋯
J1336+7550	204.0408	75.8430	15.48	14.93	1.02	0.04 ± 0.04	0.2351 ± 0.0001	0.400	0.237	0.23[a]
J1356+3840	209.0514	38.6727	17.98	15.60	1.11	0.08 ± 0.05	1.39 ± 0.01	⋯	2.679	⋯
J1410+7533	212.5899	75.5651	16.43	15.96	1.29	0.02 ± 0.07	0.852 ± 0.001	2.701	0.960	3.26[a]
J1505+8604	226.3111	86.0753	16.53	15.76	1.40	0.05 ± 0.06	1.2333 ± 0.0008	1.219	1.219	⋯
J1600+6651	240.2484	66.8511	16.47	16.25	1.18	0.09 ± 0.08	0.5137 ± 0.0002	0.578	0.604	⋯
J1649+4726	252.4820	47.4452	15.57	15.05	1.06	0.04 ± 0.04	0.2726 ± 0.0001	0.400	0.297	⋯
J1728+4303	262.0179	43.0590	16.30	15.70	1.39	0.02 ± 0.05	1.5429 ± 0.0006	1.548	1.547	1.60[b]
J1741+3026	265.4283	30.4466	16.70	15.97	1.08	0.03 ± 0.06	0.2039 ± 0.0001	0.202	0.178	0.20[a]
J1745+5414	266.3538	54.2412	16.55	15.70	1.28	0.05 ± 0.06	1.3567 ± 0.0004	1.356	1.348	1.40[b]
J1807+3637	271.7788	36.6215	16.44	15.90	1.19	0.07 ± 0.06	1.1141 ± 0.0006	1.104	1.092	⋯
J1809+2758	272.4902	27.9709	17.50	15.97	0.76	0.04 ± 0.06	2.41 ± 0.01	⋯	3.135	⋯
J1811+2409	272.8511	24.1503	16.63	15.97	1.10	0.06 ± 0.05	0.9215 ± 0.0002	0.904	0.899	⋯
J1813+3844	273.4528	38.7482	15.95	15.42	1.03	0.09 ± 0.05	0.2432 ± 0.0001	0.318	0.312	0.24[a]
J1813+4531*	273.3915	45.5216	16.60	15.80	1.11	0.05 ± 0.07	0.0931 ± 0.0001	0.238	⋯	⋯
J1846+3616	281.7226	36.2796	16.69	15.95	0.98	0.03 ± 0.06	0.1340 ± 0.0001	0.197	0.152	⋯
J1846+8425	281.7071	84.4181	15.72	15.08	0.93	0.05 ± 0.04	0.2255 ± 0.0001	0.458	0.416	0.22[a]
J1859+5130	284.9838	51.5094	16.49	15.94	1.27	0.07 ± 0.06	0.7117 ± 0.0004	0.710	0.739	⋯
J1918+4222	289.5642	42.3799	16.38	15.86	1.06	0.04 ± 0.05	0.4397 ± 0.0001	0.485	0.502	⋯
J1938+5408	294.5447	54.1489	16.57	15.79	1.08	0.06 ± 0.06	0.2717 ± 0.0001	0.273	0.289	1.00[d]
J2114+2524	318.5876	25.4062	16.32	15.59	1.11	0.04 ± 0.07	0.0897 ± 0.0001	0.239	0.205	⋯
J2115+2526*	318.9501	25.4455	16.72	15.87	1.01	0.03 ± 0.08	0.2302 ± 0.0001	0.229	⋯	⋯
J2135+3348	323.9296	33.8053	16.62	15.98	1.11	0.09 ± 0.05	0.4296 ± 0.0003	0.419	0.442	⋯
J2139+2929	324.8727	29.4961	16.65	15.92	1.09	0.05 ± 0.05	0.3803 ± 0.0001	0.381	0.360	⋯
J2206+2757	331.7160	27.9662	16.50	15.90	1.06	0.00 ± 0.07	0.2512 ± 0.0001	0.279	0.309	0.90[b]
J2217+3555	334.3668	35.9300	16.63	15.85	1.04	0.10 ± 0.07	0.1466 ± 0.0002	0.158	0.181	⋯
J2225+3952	336.4773	39.8795	16.73	15.97	1.37	0.04 ± 0.05	1.75 ± 0.01	1.747	1.745	⋯
J2232+4230	338.0374	42.5016	16.60	15.97	1.34	0.01 ± 0.05	1.1386 ± 0.0004	⋯	1.490	⋯
J2235+4431	338.9504	44.5308	16.70	15.96	1.22	0.03 ± 0.05	0.9575 ± 0.0002	⋯	1.462	⋯
J2332+2136	353.1988	21.6103	16.39	15.82	1.32	0.11 ± 0.06	1.0160 ± 0.0005	0.387	1.045	0.80[d]
J2359+8307*	359.9554	83.1212	16.40	15.71	0.97	0.11 ± 0.07	0.2861 ± 0.0001	0.285	⋯	⋯

References.
[a] Gaia DR3 QSO candidates (Gaia Collaboration et al. 2023), https://gea.esac.esa.int/archive.
[b] Bayesian high-redshift quasar classification (G. T. Richards et al. 2015).
[c] VizieR Online Data Catalog: Lick Northern Proper Motion: NPM1 Ref. Galaxies (A. R. Klemola et al. 1994).
[d] Identification of 1.4 million AGN using WISE Data (N. J. Secrest et al. 2015).

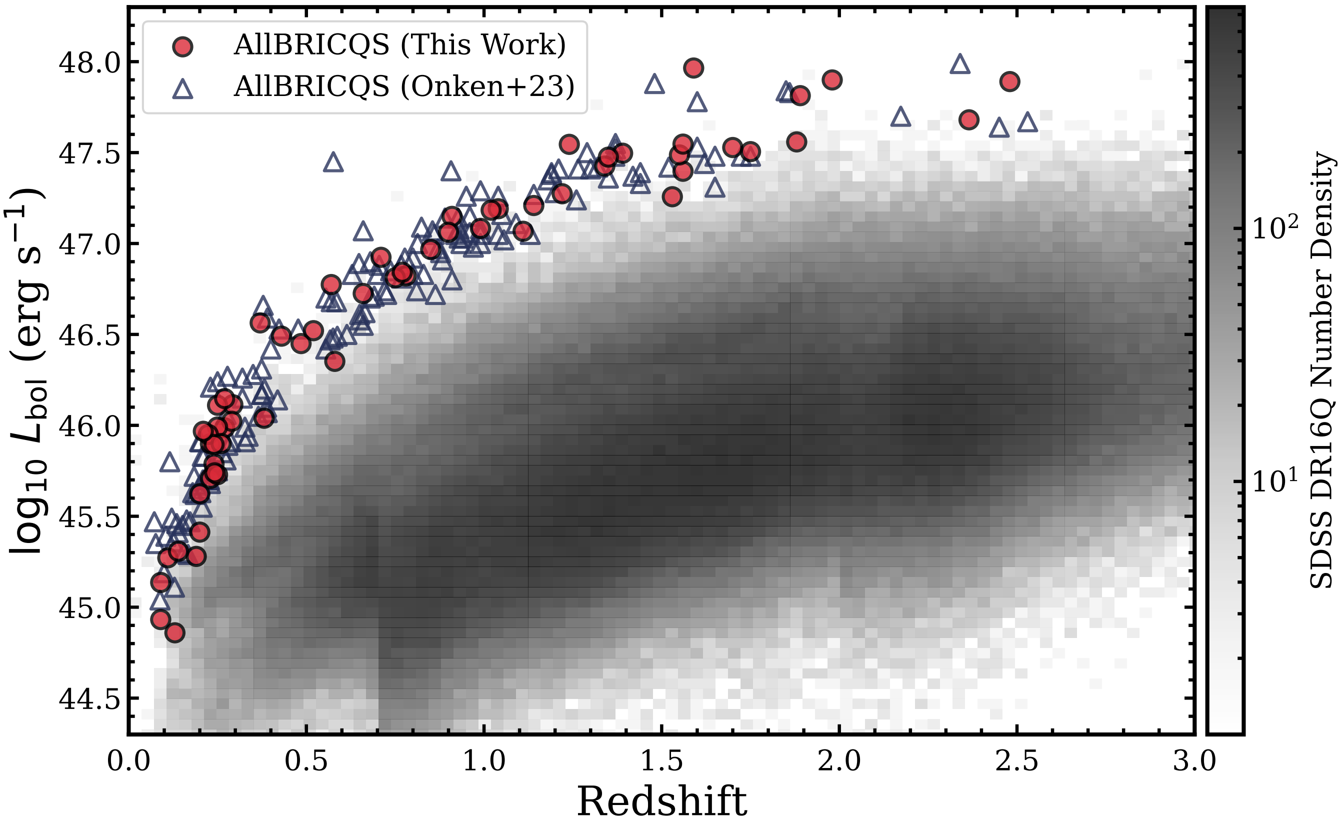

Figure 2. Distribution of redshift and bolometric luminosity for AllBRICQS quasars in this work (Northern Hemisphere; filled red circles) and from C. A. Onken et al. (2023) (Southern Hemisphere; open blue triangles), in comparison to SDSS DR16Q (B. W. Lyke et al. 2020), shown as gray contours. The AllBRICQS quasars occupy the bright end of the quasar luminosity distribution, exhibiting significantly higher luminosities than the bulk of the SDSS DR16Q sample. The gray contours correspond to a two-dimensional histogram constructed using 10,000 bins (100 bins per axis), effectively illustrating the density distribution of the SDSS quasars.

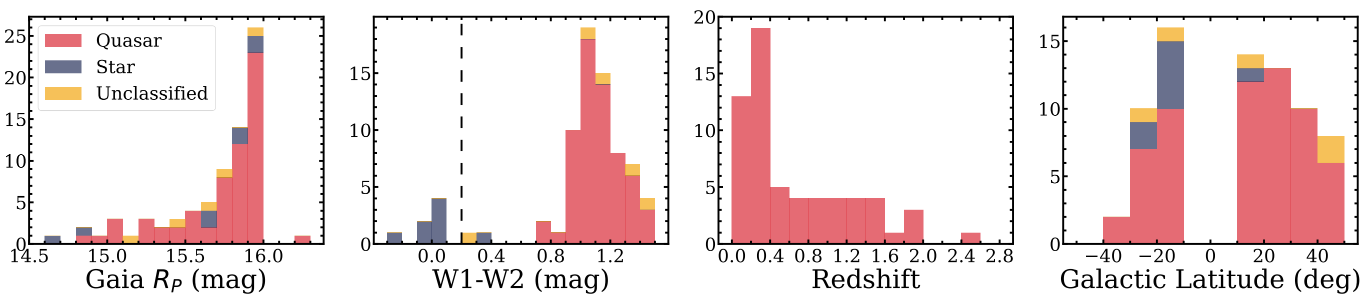

Figure 3. Distributions of key properties of the spectroscopically observed 75 sources in this study. The histograms, displayed from left to right, show Gaia R_P magnitude, W1 − W2 color, measured redshift, and Galactic latitude. The W1 − W2 color cut at 0.2 is indicated by a black dashed line. The color values are primarily sourced from the CatWISE catalog (P. R. M. Eisenhardt et al. 2020; F. Marocco et al. 2021) and supplemented with AllWISE (https://wise2.ipac.caltech.edu/docs/release/allwise/expsup/index.html) when CatWISE values are unavailable. Although the original AllBRICQS selection used AllWISE magnitudes, the color values shown here are based on CatWISE to reflect the intended selection methodology. As a result, a few objects appear below the 0.2 cut, since they were selected using AllWISE but would not have satisfied the cut under CatWISE photometry. With the exception of redshift, all other properties are derived from Gaia DR3 (Gaia Collaboration et al. 2016, 2021).

G. T. Richards et al. 2015; N. J. Secrest et al. 2015; Gaia Collaboration et al. 2023). However, none of these 62 quasars had previously been spectroscopically confirmed or had their redshifts measured. In Table 1, 62 new quasars are presented with information.

For J0919+3557, we adopted the classification as a quasar based on the publicly available DESI spectrum,[14] rather than from our own observations. This object is classified as a galaxy at $z = 0.18$ in the Dark Energy Spectroscopic Instrument (DESI) DR1 catalog (DESI Collaboration et al. 2025; M. Juneau et al. 2025, in preparation). Due to its pointlike morphology, it was classified as a star in SDSS DR18 (A. Almeida et al. 2023) and as a quasar candidate by G. T. Richards et al. (2015).

However, we determine its redshift to be $z = 2.365$, consistent with a quasar, supported by the presence of multiple foreground absorption systems. Specifically, three absorption lines at 6490, 6580, and 6600 Å correspond to an Fe II absorption system at $z = 1.769$, and a doublet at 7740 and 7770 Å corresponds to Mg II at the same redshift. Additionally, a Mg II doublet at 9190 and 9210 Å indicates a second

[14] https://www.legacysurvey.org/viewer/desi-spectrum/dr1/targetid2305843014536273669

Table 2
AllBRICQS Unclassified Sources

Target	R.A. (J2000) (deg)	Decl. (J2000) (deg)	B_P (mag)	R_P (mag)	$W12$ (mag)	μ (mas yr^{-1})	Redshift			
							AllBRICQS	Quaia	CatNorth	Others
J0219+4828	34.9536	48.4683	17.04	15.96	0.26	0.21 ± 0.11	⋯	⋯	⋯	⋯
J0712+3142	108.2353	31.7060	17.02	15.74	1.12	0.06 ± 0.09	0.72	⋯	⋯	⋯
J1040+6711	160.1677	67.1917	16.27	15.47	1.05	0.03 ± 0.04	0.74	0.474	⋯	⋯
J1418+6702	214.6939	67.0424	16.20	15.14	1.48	0.03 ± 0.05	1.80	⋯	⋯	⋯
J2330+3937	352.6161	39.6210	16.87	15.69	1.36	0.16 ± 0.07	1.90	⋯	⋯	⋯

Table 3
AllBRICQS Stars

Target	R.A. (J2000) (deg)	Decl. (J2000) (deg)	B_P (mag)	R_P (mag)	$W12$ (mag)	μ (mas yr^{-1})	Redshift			
							AllBRICQS	Quaia	CatNorth	Others
J0022+3431	5.6257	34.5267	15.66	15.67	−0.24	0.15 ± 0.07	0.00	⋯	⋯	⋯
J0140+4353	25.0324	43.8890	16.50	15.81	−0.03	0.16 ± 0.07	0.00	⋯	⋯	⋯
J0218+4534	34.6586	45.5777	16.57	15.84	0.06	0.13 ± 0.10	0.00	⋯	⋯	⋯
J0319+3309*	49.9753	33.1636	15.80	14.68	0.32	1.00 ± 0.38	0.00	⋯	⋯	⋯
J0422+2854	65.7033	28.9040	16.67	15.62	0.04	1.07 ± 0.65	0.00	⋯	⋯	⋯
J0425+3454	66.2837	34.9133	17.13	15.91	0.05	0.25 ± 0.10	0.00	⋯	⋯	⋯
J0536+5548	84.2075	55.8103	17.05	15.97	−0.03	0.15 ± 0.08	0.00	⋯	⋯	⋯
J2357+4826	359.3479	48.4369	15.67	14.84	0.00	0.92 ± 0.35	0.00	⋯	⋯	⋯

Note. Tables 1–3 provide a comprehensive overview of the confirmed AllBRICQS quasars, unclassified sources, and stars, listed in ascending order of R.A. The B_P, R_P magnitudes and proper motion (μ) are sourced from Gaia DR3 (Gaia Collaboration et al. 2016, 2021), while the W1 – W2 color (W_{12}) is derived from CatWISE2020 (F. Marocco et al. 2021) and supplemented with AllWISE data when unavailable (E. L. Wright et al. 2010). Although the initial candidate selection was based on AllWISE photometry, we report CatWISE values here to reflect the intended selection method. As a result, some sources may appear to lie below the W1 − W2 color cut at 0.2. Targets lacking CatWISE data are marked with an asterisk next to the target name. In the redshift columns, the "AllBRICQS" entry indicates our spectroscopic redshift measurements. The "Quaia" column lists estimated redshifts from the Gaia-unWISE quasar candidate catalog (K. Storey-Fisher et al. 2024), computed using a KNN model. The "CatNorth" column presents estimated redshifts from the improved Gaia DR3 quasar candidate catalog (Y. Fu et al. 2024).

absorption system at $z = 2.285$, which also includes weaker associated Fe II lines. These features suggest that the continuum source must lie at $z > 2.29$.

Adopting $z = 2.365$ aligns with two observed broad emission features that may correspond to Mg II and C III], although notably, C IV is absent. The redshift is further constrained by the presence of multiple lower-redshift absorbers and the absence of a prominent Lyman forest, implying an upper limit consistent with this redshift. One possible interpretation is that the Lyα emission is present but weak, and the C IV line is intrinsically faint. This object may therefore be classified as a weak-line quasar, a subclass of quasars characterized by unusually weak high-ionization lines. Such spectra are often attributed to a deficit in ionizing radiation, potentially due to cold accretion disks (A. Laor & S. W. Davis 2011). Notably, all high-ionization lines appear absent, while only low-ionization lines are clearly detected.

5.2. Unclassified Sources

Five sources remain unclassified as they do not exhibit clear quasar emission lines or Balmer absorption features characteristic of stellar atmospheres. Despite this, some of these sources have non-zero redshift estimates listed in Table 2, indicating a potentially high-probability redshift value.

A representative example is J1040+6711, which has a redshift estimate of $z = 0.474$ from the Quaia catalog (K. Storey-Fisher et al. 2024). However, the absence of Hα, Hβ, or [O III] emission features at expected wavelengths challenges this classification. An alternative interpretation suggests that the feature at 4868 Å could correspond to either Mg II or Lyα, implying that the source might be a broad absorption line quasar at $z = 0.74$ or a Lyman break galaxy at $z = 2.75$.

Both scenarios, however, remain speculative. If the object is at $z = 0.74$, the expected Hβ and [O III] lines at 8459 and 8713 Å are absent. Alternatively, if it is at $z = 2.75$, the expected Si II and C II absorption features at 4883 and 5004 Å are also not observed. Overall, the redshift values of these unclassified sources should be interpreted with caution, as the identification of their spectral features is uncertain.

5.3. Stellar Sources

Eight sources in the AllBRICQS sample were classified as stars and are listed in Table 3. Seven of them were initially tagged as Priority 2 targets (defined by $W1 - W2 < 0.3$, using AllWISE profile-fit magnitudes) during the quasar candidate classification process. Their parallax-to-error ratios (ϖ/σ_{ϖ}) exceed 1.71, indicating statistically significant parallax measurements. The minimum proper motion (μ) among these stars is 0.13 mas yr^{-1}. In contrast, quasars in our sample exhibit ϖ/σ_{ϖ} values that do not exceed 1.74, with the majority being negative. The maximum proper motion observed among quasars is 0.15 mas yr^{-1}, and the average is 0.06 mas yr^{-1}.

These metrics suggest that the selection purity could have been improved by applying more stringent criteria on proper motion and parallax-to-error ratio. A revised set of selection criteria is proposed in Section 7. Based on these updated criteria, J0319+3309, J0422+2854, and J2357+4826 are identified as stars with high probability, due to their high proper motion values ($\mu > 0.8$ mas yr^{-1}).

5.4. Objects of Special Interest

Identifying distinctive spectral features within the AllBRICQS sample provides valuable insights into rare quasar types and contributes to a deeper understanding of AGN diversity. Two notable examples are J1356+3840, a rare iron low-ionization broad absorption line quasar (FeLoBAL), and J0141+7307, which exhibits iron UV emission lines.

J1356+3840 is the only FeLoBAL among the 62 new AllBRICQS quasars. FeLoBALs, which constitute only ~0.3% of the quasar population (J. R. Trump et al. 2006), display absorption from both high- and low-ionization species, along with Fe II or Fe III. These objects are particularly valuable for studying quasar outflows and understanding quasar structure and host galaxy evolution (C. Villforth et al. 2019; H. Choi et al. 2022). As shown in Appendix C.1, J1356+3840 features broad Fe II absorption lines on the blue side of the Mg II emission line.

We confirm that J1356+3840 is the brightest FeLoBAL quasar identified to date. It has a bolometric luminosity of $\log L_{\rm bol} = 47.18$ erg s^{-1} at a redshift of $z = 1.39$. Near-infrared spectroscopic observations of this object were conducted by Y. Fu et al. (2025, in preparation) in 2021 using the TripleSpec instrument on the Palomar 200 inch telescope.

In addition to J1356+3840, which exhibits broad Fe II absorption lines, several quasars in our sample show prominent iron emission features. For example, in Appendix C.1, J0141+7307 at $z = 1.59$ exhibits a distinctive overlapping Fe II UV 62 and 63 emission line. Additionally, some spectra display a prominent UV 48 feature. A notable example is J1216+7948 at $z = 1.68$, where an emission line appears at 5605 Å. This UV Fe II emission suggests rich iron emission regions possibly influenced by overdense regions (R. G. Clowes et al. 2013; K. A. Harris et al. 2013).

6. Discussion

6.1. Comparison with Quaia

We compared our spectroscopically confirmed AllBRICQS quasars with the $G < 20.5$ Gaia-unWISE Quasar Catalog, Quaia (K. Storey-Fisher et al. 2024). Among the 62 spectroscopically confirmed quasars, 50 are classified as quasar candidates in Quaia. This means that the completeness of the Quaia catalog is about 81% with respect to AllBRICQS at $B_P < 16.5$ or $R_P < 16.0$ mag. None of the stars in our sample is included in the Quaia catalog, although one unclassified source (J1040+6711) is listed as a quasar candidate in Quaia.

There is a fundamental difference in selection strategy that accounts for the divergence between the two catalogs. The Priority 2 candidates were designed to probe deeper into the stellar locus to test whether any quasars might exist in the tail of the color distribution. In contrast, the Quaia catalog emphasizes selection purity by relying on known quasars to train its classification model. While Quaia is optimized to recover known types of quasars, it is less likely to discover

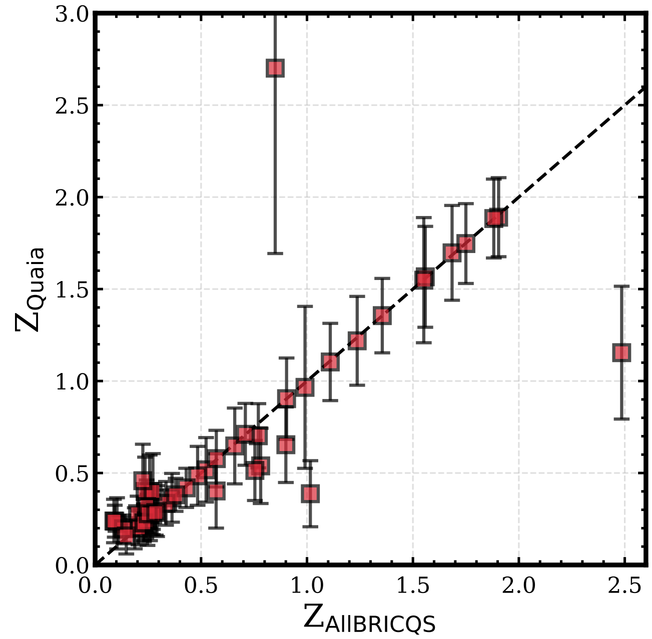

Figure 4. Comparison of redshift measurements between AllBRICQS spectroscopic values and Quaia photometric estimates. The x-axis represents the spectroscopic redshifts obtained from AllBRICQS observations, while the y-axis shows the corresponding photometric redshift estimates from the Quaia catalog.

new or unusual populations. In this study, we specifically targeted objects located near the stellar locus—those that most closely resemble quasars in color space, despite being consistent with stellar colors—and spectroscopically confirmed them to be stars.

Quaia estimates redshifts using a trained k-nearest neighbors (KNN) model that utilizes low-resolution redshift estimates from Gaia spectra along with photometric features from Gaia and WISE, offering a purely data-driven approach to quasar classification. While the Quaia catalog provides a convenient method for estimating quasar redshifts from photometric data, discrepancies with our spectroscopic measurements were noted. As shown in Figure 4, the majority of discrepancies are modest, but a few significant outliers highlight the limitations of the Quaia redshifts. We find a catastrophic failure fraction of 6% (28%) for $|\Delta z/(1 + z)| > 0.2$ (0.1). The 6% fraction at the 0.2 threshold aligns well with the 6% reported in K. Storey-Fisher et al. (2024), whereas the 28% fraction at the 0.1 threshold is notably higher than their reported 10%.

The most significant redshift discrepancy is observed in the case of J1410+7533, where the Quaia estimate differs by 1.85 from our measurement. As shown in Appendix C.1, our spectrum places this quasar at $z = 0.85$, while Quaia estimates $z = 2.7$. This discrepancy could arise from spectral line misidentification. If the emission line around 5200 Å were identified as Si IV, a redshift of 2.7 is plausible. However, at this redshift, a prominent Lyα emission line should appear near 4500 Å. The absence of this feature leads us to reject the Quaia redshift estimate of 2.7.

The second-largest discrepancy between redshift measurements is observed for J0139+4036, with a difference of $\Delta z = 1.33$. This quasar, the most distant object in the AllBRICQS-North sample, has a spectroscopic redshift of $z = 2.48$, while Quaia estimates a significantly lower photometric redshift of $z = 1.15$. At $z = 1.15$, the Mg II line would be expected around 6000 Å. However, this line is absent, and the emission features at 4800 and 5400 Å in the spectrum cannot be explained at this lower redshift.

6.2. Comparison with SDSS

By Data Release 8 (DR8; H. Aihara et al. 2011), SDSS had imaged over 14,000 deg^2 of the sky, primarily in the Northern Hemisphere. B. W. Lyke et al. (2020) provided the SDSS DR16Q catalog from the extended Baryon Oscillation Spectroscopic Survey (eBOSS), which includes spectroscopically confirmed quasars that were initially selected as candidates from imaging data. Most eBOSS quasars were selected using the CORE algorithm, which was applied to SDSS point sources with $g < 22$ or $r < 22$ (extinction corrected). These candidates were then filtered using the XDQSOz algorithm (J. Bovy et al. 2012), requiring a probability greater than 20% of being a quasar at $z > 0.9$, followed by a WISE-optical color cut to reduce stellar contamination.

Among our 62 newly confirmed quasars, 18 lie within the SDSS footprint, but are absent[15] from the SDSS DR16Q catalog. Although three of these 18 quasars are located near bright sources in the SDSS DR8 cutout images (see Appendix D), most do not show problematic photometric flags—specifically, the Q value (observation quality) and the mode value (photometric mode) are generally acceptable. The exception is J1649+4726, which has a Q value of 1, indicating poor-quality photometry. Since SDSS DR16Q does not provide completeness metrics as a function of magnitude and redshift, it is difficult to determine whether the absence of these objects is statistically expected. Moreover, it is unclear at which step(s) in the SDSS quasar selection pipeline these 18 quasars were excluded.

To compare the color trends of our quasars with those of SDSS DR16Q with $B_P < 16.5$ or $R_P < 16.0$ mag, we examined their color distributions as a function of redshift, as shown in Figure 5. In conclusion, no significant difference between the two distributions was observed. For both the R_P − W1 and W1 − W2 color distributions, the two data sets appear visually consistent across redshift, except in the bins 1.0−1.2 and 1.6−1.8, where the SDSS DR16Q sample contains only one object, making statistical interpretation unreliable.

Quantitatively, for the R_P − W1 color distribution shown in the upper panel of Figure 5, the energy distance measurement (M. L. Rizzo & G. J. Székely 2016) based on 5000 permutations yields a value of 0.0703 and a p-value of 0.9064, indicating that the two samples are statistically consistent with being drawn from the same parent population. Similarly, for the W1 − W2 distribution shown in the lower panel, the energy distance is 0.189 with a p-value of 0.9974, further supporting the conclusion that no statistically significant difference exists between the two samples.

The pentagon points in Figure 5 represent quasars from our sample that are located within the SDSS footprint and therefore could have been included in the SDSS DR16Q catalog. Most of these points are found in the redshift ranges 0−0.4 and 1.2−1.6. For both redshift intervals, considering the positions of the pentagon points and the overall trends in the optical-IR and IR color distributions, a definitive reason for their omission from the SDSS catalog is difficult to identify.

[15] J0827+5703 is classified as a QSO and has spectroscopic data available in the SDSS SkyServer DR18.

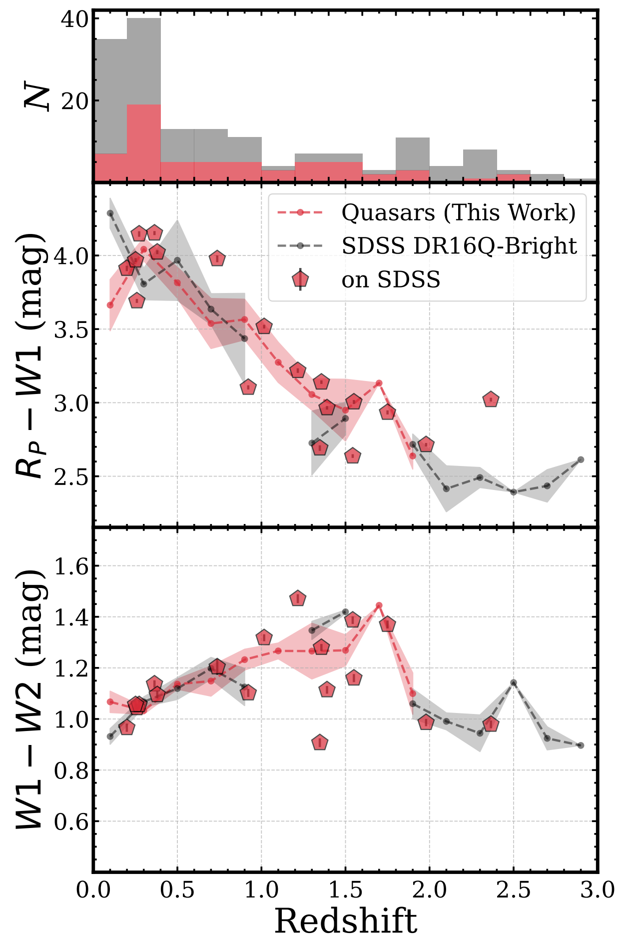

Figure 5. Distribution of R_P − W1 and W1 − W2 colors as a function of redshift. The shaded regions along the central dashed lines represent the mean color trends and the 1σ scatter within redshift bins of width 0.2. The red shaded region corresponds to our newly discovered 62 quasars, while the black shaded region corresponds to 319 SDSS DR16Q quasars (B. W. Lyke et al. 2020) that satisfy our bright selection criteria ($B_P < 16.5$ or $R_P < 16.0$ mag). Redshift bins in the SDSS sample containing only a single data point within $z < 2.0$ were excluded. Red pentagons denote the 18 quasars located within the SDSS footprint.

6.3. Comparison with DESI

The DESI Legacy Imaging Surveys Data Release 8 (K. J. Duncan 2022) covers approximately 19,000 deg^2, primarily in the Northern Hemisphere. DESI selects quasar candidates using photometric imaging in three optical bands (g, r, z) from the Legacy Imaging Surveys and two infrared bands (W1, W2) from WISE, applying a random forest algorithm to identify candidates in the magnitude range $16.5 < r < 23$ (AB mag) (E. Chaussidon et al. 2023).

Twenty-two of our 62 quasars lie within this footprint. The recent DESI DR1 catalog (DESI Collaboration et al. 2025; M. Juneau et al. 2025, in preparation) classifies 10 of our 62 quasars as confirmed quasars. Our redshift estimates are in excellent agreement with those in DESI DR1, with none of the 10 matched sources exhibiting a redshift difference greater than 0.01, except for J1216+7948 at $z = 1.68$. For this object, the redshift difference is $\Delta z = 0.016$, which can be attributed to the Mg II emission line being affected by telluric absorption, making its peak difficult to identify precisely.

Most of our quasars (48 out of 62) are brighter than the DESI lower magnitude cut of $r = 16.5$ AB mag. However, all

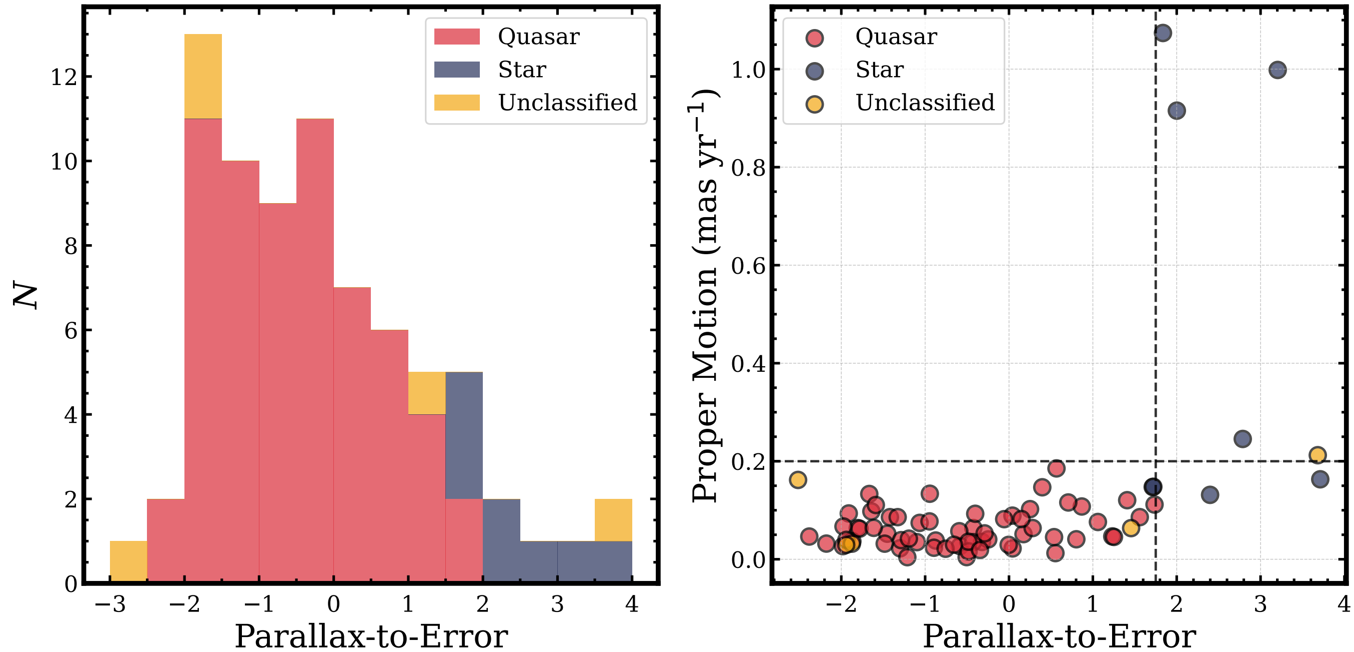

Figure 6. Distribution of the 75 observed sources in the AllBRICQS sample, with all astrometric properties derived from Gaia DR3 (Gaia Collaboration et al. 2016, 2021). (Left) Histogram of the parallax-to-error ratio, ϖ/σ_{ϖ}. Quasars (red) do not exceed a value of 2.0, with many exhibiting negative values, which correspond to near-zero parallaxes in reality (see Section 5.2 and Figure 6 of L. Lindegren et al. 2018). Stars (navy) all have $\varpi/\sigma_{\varpi} > 1.5$. (Right) Scatter plot of proper motion μ vs. parallax-to-error ratio. The dashed lines indicate the newly proposed stringent criteria for quasar selection.

10 overlapping quasars reported in the DESI catalog do not satisfy the $r > 16.5$ AB mag criterion based on our spectroscopic flux levels. Given the intrinsic variability of quasars, photometric fluxes may vary across observing epochs, making it difficult to determine why certain objects were excluded from the DESI candidate list.

7. Summary and Conclusion

We present the second installment of the AllBRICQS, targeting the identification of optically bright quasars in the Northern Hemisphere. Utilizing all-sky data from WISE and Gaia DR3, we applied the same four efficient selection criteria from C. A. Onken et al. (2023) and conducted spectroscopic observations of 75 candidates using the BOAO 1.8 m, LJO 2.4 m, and XLO 2.16 m telescopes. These observations resulted in the confirmation of 62 quasars, extending the success of the AllBRICQS methodology to the northern sky.

The newly discovered quasars span redshifts of $0.09 < z < 2.48$ and bolometric luminosities from $\log L_{\mathrm{bol}} = 44.9$ to $48.0\,\mathrm{erg\,s^{-1}}$, placing them at the luminous end of the quasar population. The purity of our Priority 1 sample, defined by $W1 - W2 > 0.3$ mag, is exceptionally high at 98.4%. Most contaminants are associated with the Priority 2 sample, which targets sources deeper within the stellar locus. As shown in Figure 6, we demonstrate that a more stringent cut on proper motion ($\mu < 0.2\,\mathrm{mas\,yr^{-1}}$) and parallax-to-error ratio ($\varpi/\sigma_{\varpi} < 1.75$) can further improve selection purity.

Our analysis also highlights the limitations of current catalogs, such as Quaia and SDSS DR16Q, in recovering bright quasars. Quaia fails to include 12 of our 62 confirmed quasars and shows significant redshift discrepancies in several cases. Similarly, 18 of our new quasars are absent from SDSS DR16Q despite lying within its imaging footprint and satisfying its brightness criteria. These omissions emphasize the continued need for spectroscopic confirmation to achieve a truly complete census of luminous quasars.

Among our discoveries are rare and notable objects, including the most luminous FeLoBAL quasar to date. The AllBRICQS-North sample will serve as a valuable resource for studies of quasar physics, BH growth, feedback processes, and host galaxy properties, particularly in regimes inaccessible to deeper but narrower surveys.

In summary, this work affirms the effectiveness of the AllBRICQS selection method and reinforces the importance of spectroscopic follow-up in uncovering the full population of the Universe's brightest AGN.

Acknowledgments

This work was supported by the National Research Foundation of Korea (NRF) grant No. 2021M3F7A1084525, funded by the Korean government (MSIT). We also made use of data obtained at the Bohyunsan Optical Astronomy Observatory, which is operated by the Korea Astronomy and Space Science Institute.

We acknowledge the support of the staff of the Xinglong 2.16 m telescope. This work was partially supported by the National Astronomical Observatories, Chinese Academy of Sciences. We also acknowledge the support of the staff of the Lijiang 2.4 m telescope. Funding for the Lijiang telescope has been provided by the Chinese Academy of Sciences and the People's Government of Yunnan Province.

This work has made use of data from the European Space Agency (ESA) mission Gaia,[16] processed by the Gaia Data Processing and Analysis Consortium (DPAC).[17] Funding for DPAC has been provided by national institutions, in particular,

[16] https://www.cosmos.esa.int/gaia
[17] https://www.cosmos.esa.int/web/gaia/dpac/consortium

the institutions participating in the Gaia Multilateral Agreement.

This publication also makes use of data products from WISE, which is a joint project of the University of California, Los Angeles, and the Jet Propulsion Laboratory/California Institute of Technology, funded by the National Aeronautics and Space Administration (NASA).

We additionally used data obtained with the Samuel Oschin 48 inch and the 60 inch telescopes at Palomar Observatory as part of the ZTF project. ZTF is supported by the National Science Foundation under grant No. AST-1440341 and by a collaboration including Caltech, IPAC, the Weizmann Institute for Science, the Oskar Klein Center at Stockholm University, the University of Maryland, the University of Washington (UW), Deutsches Elektronen-Synchrotron and Humboldt University, Los Alamos National Laboratories, the TANGO Consortium of Taiwan, the University of Wisconsin at Milwaukee, and Lawrence Berkeley National Laboratory. Operations are conducted by Caltech Optical Observatories, IPAC, and UW.

Y.C., M.I., S.W.C., H.C., M.J., and J.H.K. acknowledge support from NRF grant No. 2021M3F7A1084525. S.W.C. also acknowledges support from the Basic Science Research Program through the NRF, funded by the Ministry of Education (grant No. RS-2023-00245013). H.C. acknowledges support from NRF grant No. RS-2025-00573214 funded by the Korean government (MSIT). J.H.K. also acknowledges support from NRF grant No. 2020R1A2C3011091 and from the Institute of Information & Communications Technology Planning & Evaluation (IITP) grant No. RS-2021-II212068, funded by the Korean government (MSIT). G.L. acknowledges support from the Basic Science Research Program through the NRF, funded by MSIT (grant No. 2022R1A6A3A01085930). Y.K. was supported by NRF grant No. 2021R1C1C2091550, funded by the Korean government (MSIT). G.S.H.P. acknowledges support from the Pan-STARRS project, which is operated by the Institute for Astronomy of the University of Hawaii and supported by NASA's Near-Earth Object Observation Program under grants 80NSSC18K0971, NNX14AM74G, NNX12AR65G, NNX13AQ47G, NNX08AR22G, and 80NSSC21K1572, as well as by the State of Hawaii. T.K. and J.S. are supported by the NRF grant funded by the Korean government (MSIT) (grant No. RS-2023-00210597). D.K. acknowledges support from NRF grant No. 2021R1C1C-1013580, funded by the Korean government (MSIT).

Data Availability

The spectral data and tables presented in this paper are publicly available. An example of the spectrum data is provided in Appendix E.

Appendix A
ZTF Magnitudes of AllBRICQS Quasars

Table 4 presents the synthetic photometry results in the ZTF DR22 g- and r-filters (E. C. Bellm et al. 2019; F. J. Masci et al. 2019). A detailed explanation of the flux-scaling process is provided in Section 4.2. For J0324+2432, J0602+4743, J0633+6225, and J2115+2526, which were observed with XLT, the spectra were scaled using the ZTF g-filter magnitudes.

Table 4
ZTF Synthetic Photometry Magnitude of Quasars

Target	R.A. (J2000) (deg)	Decl. (J2000) (deg)	g (AB mag)	r (AB mag)
J0002+2529	0.6584	25.4906	16.241 ± 0.067	15.488 ± 0.034
J0052+4721	13.1842	47.3663	16.895 ± 0.104	16.423 ± 0.064
J0105+5137	16.4816	51.6293	16.972 ± 0.150	16.496 ± 0.086
J0139+4036	24.7536	40.6120	16.210 ± 0.069	16.278 ± 0.060
J0141+7307	25.3294	73.1285	17.224 ± 0.221	16.300 ± 0.077
J0152+3143	28.0699	31.7171	16.794 ± 0.071	16.366 ± 0.039
J0212+3306	33.2025	33.1120	17.380 ± 0.125	17.207 ± 0.102
J0214+3824	33.6604	38.4148	16.642 ± 0.048	16.450 ± 0.040
J0245+7718	41.3216	77.3059	17.687 ± 0.127	16.700 ± 0.052
J0303+2629	45.7550	26.4884	16.676 ± 0.054	16.333 ± 0.033
J0324+2432	51.1758	24.5459	16.667 ± 0.143	16.162 ± 0.086
J0503+8351	75.7822	83.8612	16.627 ± 0.060	16.266 ± 0.036
J0528+6633	82.1957	66.5598	16.794 ± 0.066	16.39 ± 0.038
J0602+4743	90.5840	47.7324	16.926 ± 0.268	16.500 ± 0.162
J0633+6225	98.2560	62.4288	16.602 ± 0.146	16.285 ± 0.101
J0643+5044	100.9192	50.7418	15.942 ± 0.037	15.661 ± 0.025
J0653+6716	103.3123	67.2795	16.264 ± 0.047	15.969 ± 0.030
J0707+2821	106.9702	28.3518	16.290 ± 0.113	15.936 ± 0.075
J0708+7555	107.0917	75.9217	16.575 ± 0.057	16.425 ± 0.040
J0708+7822	107.0212	78.3713	15.741 ± 0.034	15.672 ± 0.026
J0728+2056	112.1122	20.9385	17.162 ± 0.211	16.428 ± 0.100
J0750+7751	117.7125	77.8504	16.148 ± 0.043	16.206 ± 0.035
J0807+7550	121.8778	75.8388	15.904 ± 0.037	15.593 ± 0.024
J0827+5703	126.9324	57.0606	17.195 ± 0.128	16.548 ± 0.062
J0919+3557	139.9281	35.9514	17.013 ± 0.076	16.314 ± 0.038
J0919+7539	139.9001	75.6623	16.286 ± 0.043	16.211 ± 0.035
J0938+4927	144.7180	49.4584	16.364 ± 0.045	16.329 ± 0.038
J1143+7727	175.8681	77.4592	16.752 ± 0.059	16.449 ± 0.041

Table 4
(Continued)

Target	R.A. (J2000) (deg)	Decl. (J2000) (deg)	g (AB mag)	r (AB mag)
J1203+7226	180.7783	72.4370	16.141 ± 0.040	15.895 ± 0.030
J1216+7948	184.1664	79.8003	17.373 ± 0.093	16.697 ± 0.047
J1256+5404	194.1117	54.0742	16.596 ± 0.055	16.364 ± 0.040
J1317+8637	199.3724	86.6268	16.904 ± 0.072	16.346 ± 0.043
J1336+7550	204.0408	75.8430	15.641 ± 0.027	15.498 ± 0.021
J1356+3840	209.0514	38.6727	18.653 ± 0.273	16.697 ± 0.047
J1410+7533	212.5899	75.5651	16.332 ± 0.040	16.438 ± 0.035
J1505+8604	226.3111	86.0753	16.331 ± 0.047	16.030 ± 0.035
J1600+6651	240.2484	66.8511	16.561 ± 0.050	16.499 ± 0.040
J1649+4726	252.4820	47.4452	15.784 ± 0.031	15.600 ± 0.023
J1728+4303	262.0179	43.0590	16.688 ± 0.054	16.259 ± 0.034
J1741+3026	265.4283	30.4466	16.795 ± 0.059	16.531 ± 0.040
J1745+5414	266.3538	54.2412	17.263 ± 0.082	16.271 ± 0.034
J1807+3637	271.7788	36.6215	17.138 ± 0.075	16.577 ± 0.041
J1809+2758	272.4902	27.9709	18.154 ± 0.035	16.840 ± 0.006
J1811+2409	272.8511	24.1503	16.753 ± 1.236	16.300 ± 0.767
J1813+3844	273.4528	38.7482	16.117 ± 0.068	16.062 ± 0.061
J1813+4531	273.3915	45.5216	17.040 ± 0.072	16.160 ± 0.033
J1846+3616	281.7226	36.2796	17.484 ± 0.188	16.753 ± 0.104
J1846+8425	281.7071	84.4181	15.931 ± 0.037	15.713 ± 0.029
J1859+5130	284.9838	51.5094	16.306 ± 0.077	16.187 ± 0.065
J1918+4222	289.5642	42.3799	16.265 ± 1.085	16.200 ± 0.960
J1938+5408	294.5447	54.1489	16.570 ± 0.073	16.383 ± 0.059
J2114+2524	318.5876	25.4062	16.378 ± 0.068	16.038 ± 0.049
J2115+2526	318.9501	25.4455	17.142 ± 0.276	16.632 ± 0.174
J2135+3348	323.9296	33.8053	16.363 ± 0.046	16.260 ± 0.041
J2139+2929	324.8727	29.4961	16.611 ± 0.054	16.369 ± 0.044
J2206+2757	331.7160	27.9662	16.940 ± 0.031	16.700 ± 0.025
J2217+3555	334.3668	35.9300	16.651 ± 0.079	16.467 ± 0.065
J2225+3952	336.4773	39.8795	16.873 ± 0.058	16.600 ± 0.045
J2232+4230	338.0374	42.5016	16.920 ± 0.068	16.550 ± 0.038
J2235+4431	338.9504	44.5308	16.854 ± 0.085	16.450 ± 0.060
J2332+2136	353.1988	21.6103	16.578 ± 0.092	16.328 ± 0.071
J2359+8307	359.9554	83.1212	16.674 ± 0.060	16.453 ± 0.040

Appendix B
AllBRICQS Luminosities

In Table 5, we present the continuum and bolometric luminosities for the confirmed AllBRICQS quasars, arranged in ascending order of R.A. Two quasars, J0633+6225 and J1809+2758, are not included in the table due to insufficient wavelength coverage for reliable luminosity estimation. Only valid data points are used in the analysis, and when multiple continuum luminosities are available, we adopt the mean value. Additional details on the bolometric luminosity calculation are provided in Section 4.4.

For J1859+5130 at $z = 0.71$, although both the 3000 and 5100 Å continuum regions are covered, only the 3000 Å luminosity is used in the bolometric correction. This decision is based on unreliable flux measurements at $\lambda \gtrsim 7500$ Å in the spectrum obtained on UT 2022 October 27.

Table 5
Bolometric and Continuum Luminosities of Quasars

Target	$\log(L_{\rm bol})$ (erg s^{-1})	$\log(L_{1450\,Å})$ (erg s^{-1})	$\log(L_{3000\,Å})$ (erg s^{-1})	$\log(L_{5100\,Å})$ (erg s^{-1})
J0002+2529	46.49	⋯	⋯	45.62
J0052+4721	47.04	⋯	46.35	⋯
J0105+5137	46.86	⋯	46.17	⋯
J0139+4036	47.46	46.94	⋯	⋯
J0141+7307	47.69	⋯	47.01	⋯
J0152+3143	47.27	⋯	46.59	⋯
J0212+3306	45.37	⋯	⋯	44.39
J0214+3824	47.12	⋯	46.42	⋯
J0245+7718	47.48	⋯	46.80	⋯
J0303+2629	46.96	⋯	46.26	⋯
J0324+2432	45.96	⋯	⋯	45.03
J0503+8351	45.95	⋯	⋯	45.02
J0528+6633	46.65	⋯	⋯	45.79
J0602+4743	45.91	⋯	⋯	44.98
J0643+5044	46.00	⋯	⋯	45.08
J0653+6716	46.15	⋯	⋯	45.24
J0707+2821	47.52	⋯	46.84	⋯
J0708+7555	47.24	⋯	46.55	⋯
J0708+7822	46.10	⋯	⋯	45.19
J0728+2056	47.09	⋯	46.40	⋯
J0750+7751	46.78	⋯	46.08	⋯
J0807+7550	46.76	⋯	⋯	45.91
J0827+5703	47.21	⋯	46.52	⋯
J0919+3557	47.68	47.18	⋯	⋯
J0919+7539	46.39	⋯	⋯	45.50
J0938+4927	46.63	⋯	45.98	45.72
J1143+7727	46.84	⋯	46.14	⋯
J1203+7226	45.35	⋯	⋯	44.36
J1216+7948	47.17	⋯	46.48	⋯
J1256+5404	45.67	⋯	⋯	44.71
J1317+8637	45.98	⋯	⋯	45.06
J1336+7550	46.11	⋯	⋯	45.20
J1356+3840	47.18	⋯	46.49	⋯
J1410+7533	46.78	⋯	46.07	⋯
J1505+8604	47.27	⋯	46.58	⋯
J1600+6651	46.41	⋯	⋯	45.52
J1649+4726	46.18	⋯	⋯	45.28
J1728+4303	47.19	⋯	46.50	⋯
J1741+3026	45.63	⋯	⋯	44.67
J1745+5414	47.15	⋯	46.46	⋯
J1807+3637	46.81	⋯	46.11	⋯
J1811+2409	46.90	⋯	46.20	⋯
J1813+3844	45.92	⋯	⋯	44.99
J1813+4531	44.94	⋯	⋯	43.92
J1846+3616	45.22	⋯	⋯	44.22
J1846+8425	46.04	⋯	⋯	45.12
J1859+5130	46.73	⋯	46.03	45.40
J1918+4222	46.45	⋯	⋯	45.57
J1938+5408	45.97	⋯	⋯	45.05
J2114+2524	45.18	⋯	⋯	44.18
J2115+2526	45.69	⋯	⋯	44.74
J2135+3348	46.39	⋯	⋯	45.50
J2139+2929	46.24	⋯	⋯	45.33
J2206+2757	45.78	⋯	⋯	44.84
J2217+3555	45.47	⋯	⋯	44.50
J2225+3952	47.14	⋯	46.45	⋯
J2232+4230	46.94	⋯	46.24	⋯
J2235+4431	46.96	⋯	46.26	⋯
J2332+2136	46.93	⋯	46.24	⋯
J2359+8307	46.04	⋯	⋯	45.11

Appendix C
Gallery of AllBRICQS Observed Spectra

C.1. Gallery of AllBRICQS Quasar Spectra

Figure 7 presents the spectra of the AllBRICQS quasars, arranged in order of ascending redshift. Spectra with incomplete wavelength coverage correspond to targets observed with either XLT or LJT, where partial spectral data were obtained.

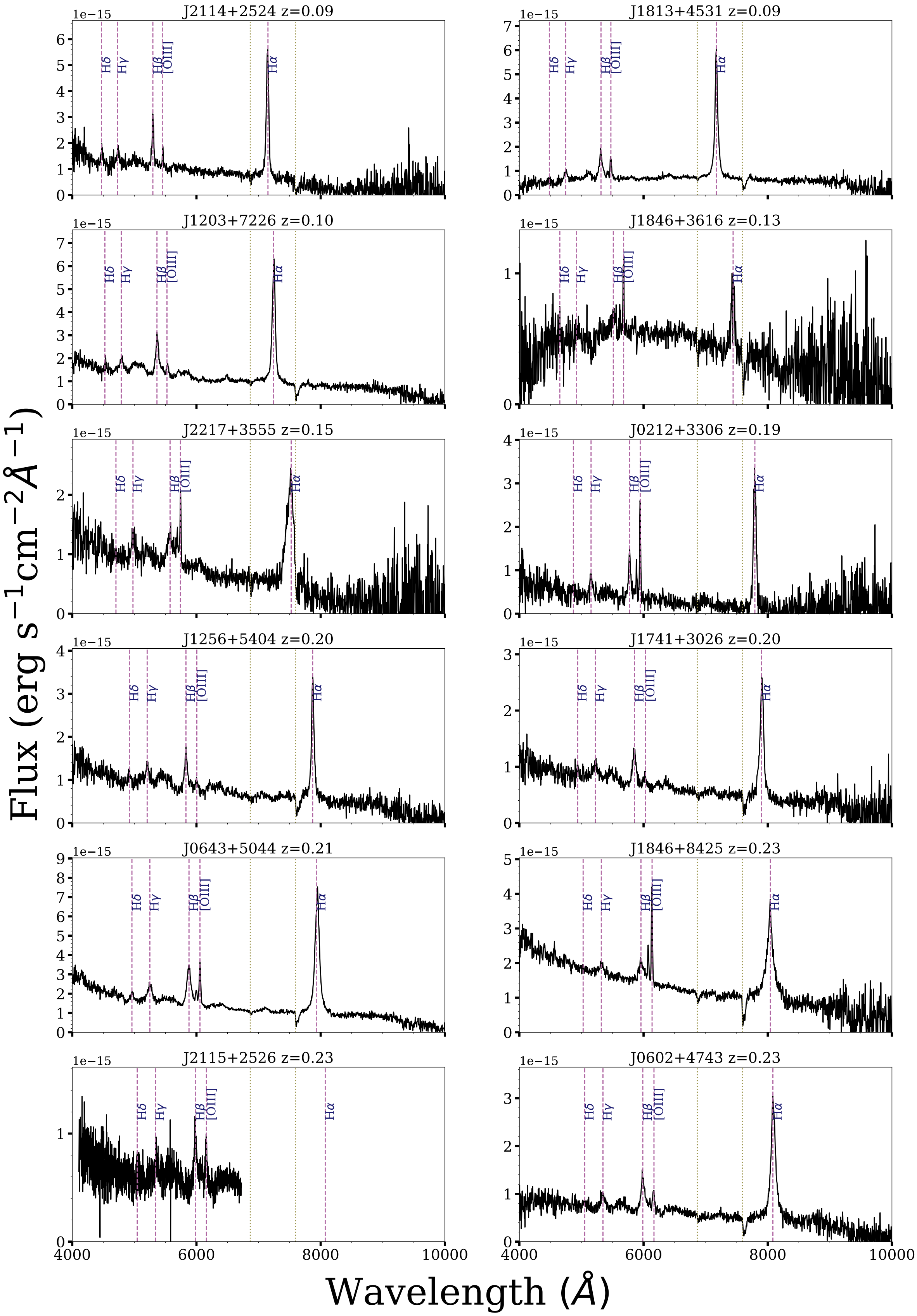

Figure 7. Spectra of the AllBRICQS Northern Hemisphere quasar sample, displayed in order of increasing redshift. Each panel is labeled with the target name and the redshift measured from the observed spectrum. The *y*-axis shows the scaled flux, aligned with contemporaneous broadband photometry. Pink dotted vertical lines indicate the positions of key quasar emission features, with line identifications shown to the right of each marker. Green dotted vertical lines at 6867.2 and 7593.7 Å mark regions affected by telluric absorption, which may impact spectral interpretation.

(The complete figure set (5 images) is available in the online article.)

C.2. Unclassified Sources Observed in AllBRICQS

Figure 8 presents the spectra of the AllBRICQS unclassified sources, arranged in order of ascending R.A. Spectra with incomplete wavelength coverage correspond to targets observed with either XLT or LJT, where partial spectral data were obtained.

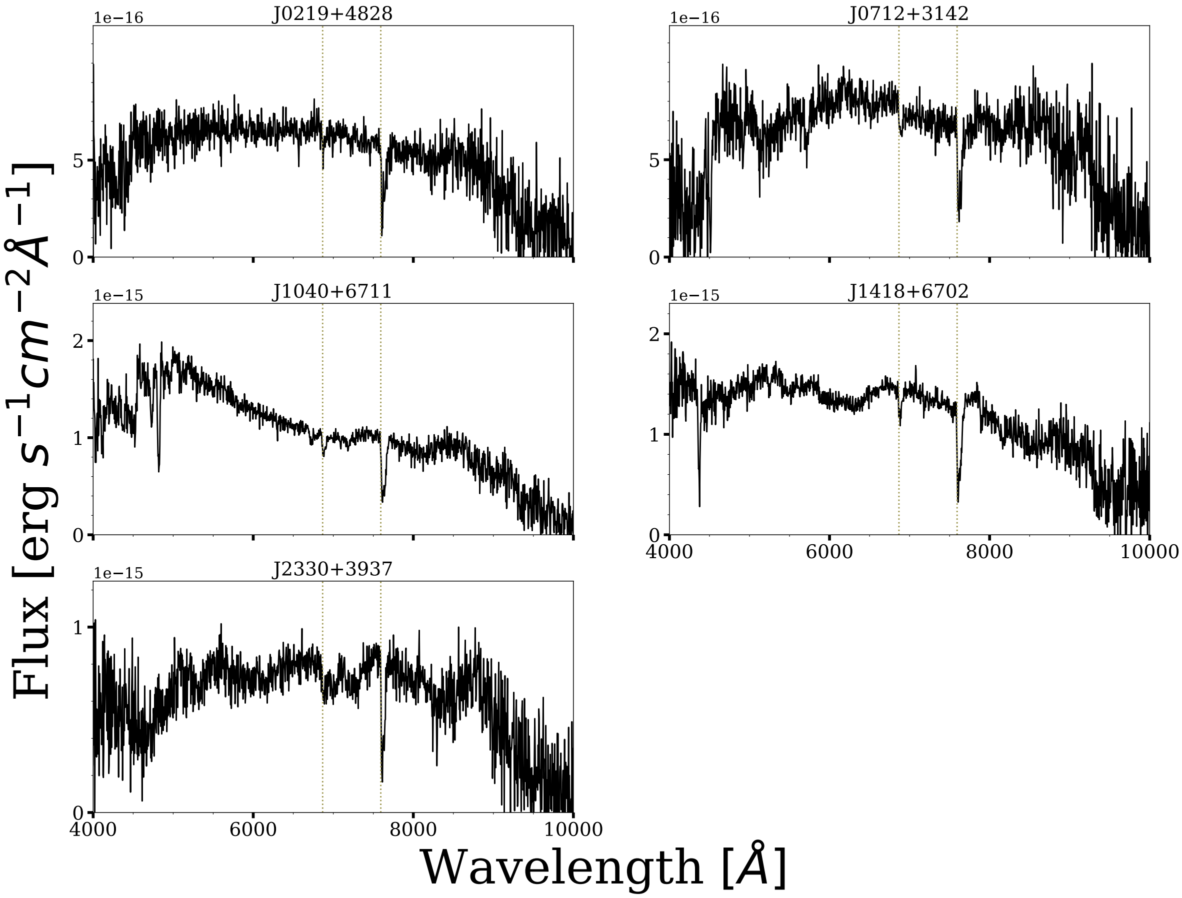

Figure 8. Spectra of the unclassified sources, presented in order of increasing R.A. The *y*-axis shows the scaled flux, aligned with contemporaneous broadband photometry. Green dotted vertical lines at 6867.2 and 7593.7 Å mark regions affected by telluric absorption, which may impact spectral interpretation.

C.3. Stars Observed in AllBRICQS

Figure 9 presents the spectra of the AllBRICQS stars, arranged in order of ascending R.A. Spectra with incomplete wavelength coverage correspond to targets observed with either XLT or LJT, where partial spectral data were obtained.

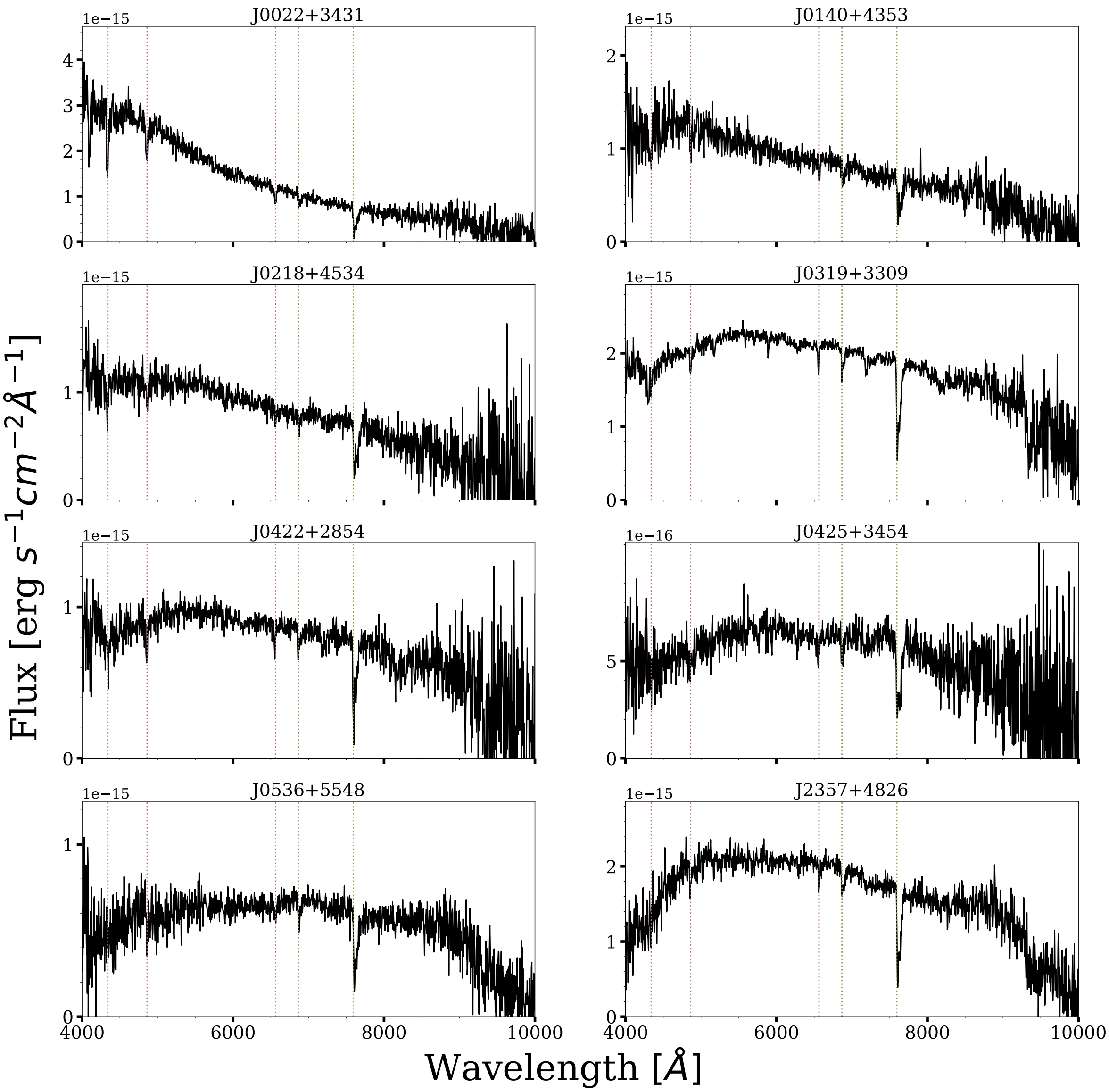

Figure 9. Spectra of the stars, presented in order of increasing R.A. The *y*-axis shows the scaled flux, aligned with contemporaneous broadband photometry. Pink dotted vertical lines indicate the positions of Balmer absorption lines. Green dotted vertical lines at 6867.2 and 7593.7 Å mark regions affected by telluric absorption, which may impact spectral interpretation.

Appendix D
Quasars on SDSS Footprint

Figure 10 shows the gallery of 18 quasars located within the SDSS footprint (R. Ahumada et al. 2020).

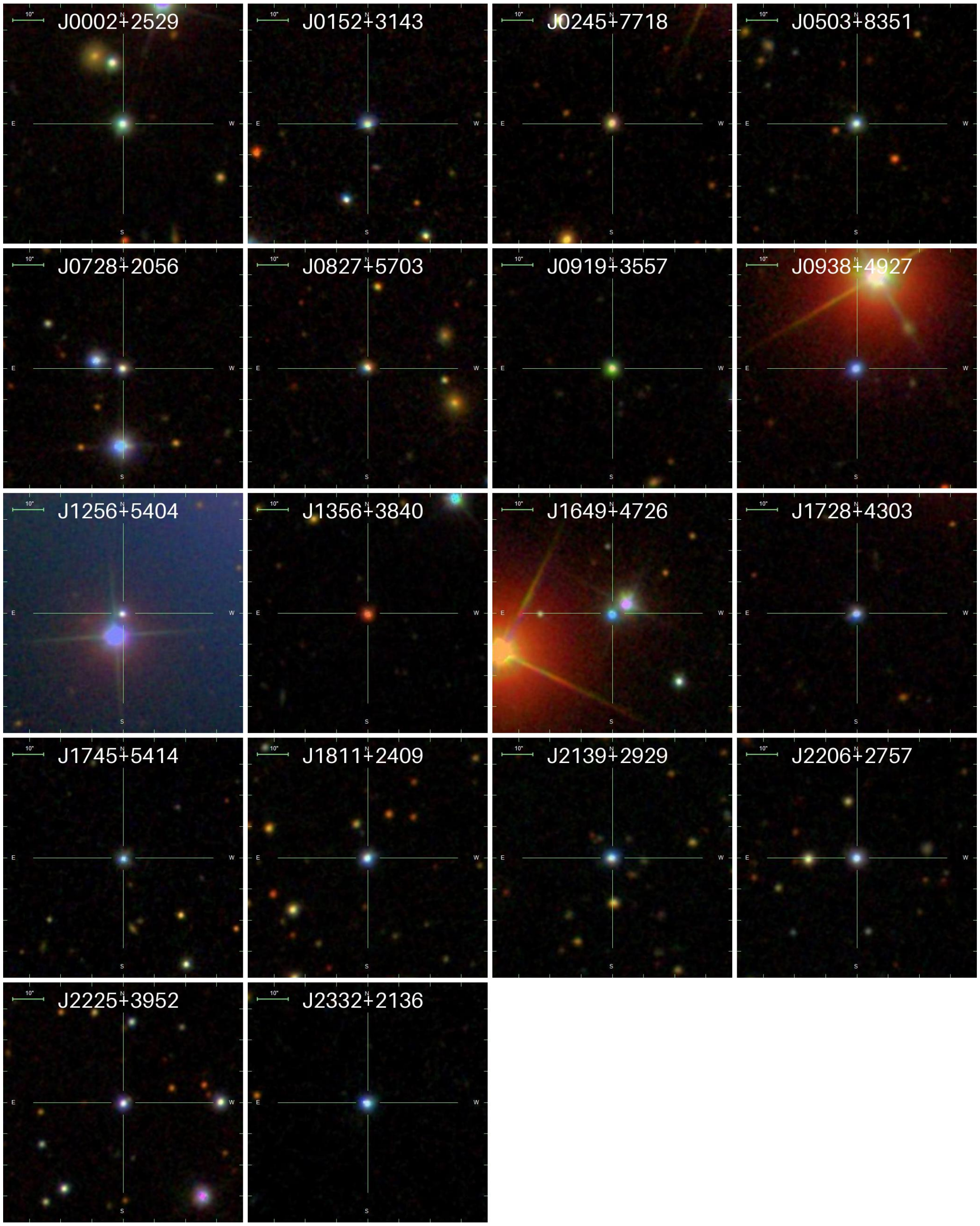

Figure 10. Cutout images of 18 newly discovered quasars that lie within the SDSS footprint but are not included in the SDSS DR16Q catalog (B. W. Lyke et al. 2020). The name of each quasar is displayed at the top of its respective panel. A scale bar indicating 10″ is shown in the upper left corner of each panel.

Appendix E
Optical Spectra

An example of the optical spectrum data is shown in Table 6, which provides a partial excerpt of the spectrum for J2114+2524 in ASCII format. The full optical spectra of all 62 quasars are available in a machine-readable format.

Table 6
Spectrum of J2114+2524

λ (Å)	f_λ (erg s^{-1} cm^{-2} Å^{-1})	f_λ Uncertainty (erg s^{-1} cm^{-2} Å^{-1})
4002.4	1.588E-15	2.061E-16
4006.9	1.211E-15	2.035E-16
4011.4	2.161E-15	2.010E-16
4016.0	1.153E-15	1.901E-16
4020.5	1.454E-15	1.962E-16
4025.0	9.426E-16	1.961E-16
4029.5	8.905E-16	1.857E-16
4034.1	1.462E-15	1.877E-16
4038.6	2.312E-15	1.997E-16
4043.1	1.464E-15	1.878E-16

(This table is available in its entirety in machine-readable form in the online article.)

ORCID iDs

Yunyi Choi https://orcid.org/0009-0000-2050-1118
Yuming Fu https://orcid.org/0000-0002-0759-0504
Myungshin Im https://orcid.org/0000-0002-8537-6714
Xue-Bing Wu https://orcid.org/0000-0002-7350-6913
Christopher A. Onken https://orcid.org/0000-0003-0017-349X
Christian Wolf https://orcid.org/0000-0002-4569-016X
Seo-Won Chang https://orcid.org/0000-0002-3118-8275
Hyeonho Choi https://orcid.org/0000-0003-4422-6426
Mankeun Jeong https://orcid.org/0009-0003-1280-0099
Yongjung Kim https://orcid.org/0000-0003-1647-3286
Gu Lim https://orcid.org/0000-0002-5760-8186
Yuxuan Pang https://orcid.org/0009-0005-3823-9302
Taewan Kim https://orcid.org/0009-0001-3758-9440
Jubee Sohn https://orcid.org/0000-0002-9254-144X
Dohyeong Kim https://orcid.org/0000-0002-6925-4821
Ji Hoon Kim https://orcid.org/0000-0002-1418-3309
Eunhee Ko https://orcid.org/0000-0002-8130-8044
Gregory S. H. Paek https://orcid.org/0000-0002-6639-6533
Sungho Jung https://orcid.org/0009-0009-5870-4266

References

Ahumada, R., Allende Prieto, C., Almeida, A., et al. 2020, ApJS, 249, 3
Aihara, H., Allende Prieto, C., An, D., et al. 2011, ApJS, 193, 29
Almeida, A., Anderson, S. F., Argudo-Fernández, M., et al. 2023, ApJS, 267, 44
Becker, R. H., White, R. L., Gregg, M. D., et al. 2001, ApJS, 135, 227
Bellm, E. C., Kulkarni, S. R., Graham, M. J., et al. 2019, PASP, 131, 018002
Bentz, M. C., Denney, K. D., Grier, C. J., et al. 2013, ApJ, 767, 149
Bohlin, R. C., Gordon, K. D., & Tremblay, P. E. 2014, PASP, 126, 711
Bohlin, R. C., Hubeny, I., & Rauch, T. 2020, AJ, 160, 21
Bovy, J., Myers, A. D., Hennawi, J. F., et al. 2012, ApJ, 749, 41
Chaussidon, E., Yèche, C., Palanque-Delabrouille, N., et al. 2023, ApJ, 944, 107
Choi, H., Leighly, K. M., Terndrup, D. M., et al. 2022, ApJ, 937, 74
Clowes, R. G., Raghunathan, S., Söchting, I. K., Graham, M. J., & Campusano, L. E. 2013, MNRAS, 433, 2467
DESI Collaboration, Abdul-Karim, M., Adame, A. G., et al. 2025, arXiv:2503.14745
Dopita, M., Hart, J., McGregor, P., et al. 2007, Ap&SS, 310, 255
Dopita, M., Rhee, J., Farage, C., et al. 2010, Ap&SS, 327, 245
Duncan, K. J. 2022, MNRAS, 512, 3662
Eisenhardt, P. R. M., Marocco, F., Fowler, J. W., et al. 2020, ApJS, 247, 69
Evans, D. W., Riello, M., D. Angeli, F., et al. 2018, A&A, 616, A4
Fan, Z., Wang, H., Jiang, X., et al. 2016, PASP, 128, 115005
Fitzpatrick, E. L. 1999, PASP, 111, 63
Flesch, E. W. 2021, arXiv:2105.12985
Flesch, E. W. 2023, OJAp, 6, 49
Fu, Y., & Li, Y., 2024 PyFOSC: A Pipeline Toolbox for BFOSC/YFOSC Long-slit Spectroscopy Data Reduction, v1.1.0,, Zenodo, doi:10.5281/zenodo.10967240
Fu, Y., Wu, X.-B., Jiang, L., et al. 2022, ApJS, 261, 32
Fu, Y., Wu, X.-B., Li, Y., et al. 2024, ApJS, 271, 54
Gaia Collaboration, Bailer-Jones, C. A. L., Teyssier, D., et al. 2023, A&A, 674, A41
Gaia Collaboration, Brown, A. G. A., Vallenari, A., et al. 2021, A&A, 649, A1
Gaia Collaboration, Prusti, T., de Bruijne, J. H. J., et al. 2016, A&A, 595, A1
GRAVITY Collaboration, Sturm, E., Dexter, J., et al. 2018, Natur, 563, 657
GRAVITY Collaboration, Amorim, A., Bauböck, M., et al. 2020, A&A, 643, A154
GRAVITY Collaboration, Amorim, A., Bauböck, M., et al. 2021a, A&A, 648, A117
GRAVITY Collaboration, Amorim, A., Bauböck, M., et al. 2021b, A&A, 654, A85
Guo, H., Shen, Y., & Wang, S., 2018 PyQSOFit: Python code to fit the spectrum of quasars, Astrophysics Source Code Library,, ascl:1809.008
Hagen, H. J., Groote, D., Engels, D., & Reimers, D. 1995, A&AS, 111, 195
Hamuy, M., Suntzeff, N. B., Heathcote, S. R., et al. 1994, PASP, 106, 566
Hamuy, M., Walker, A. R., Suntzeff, N. B., et al. 1992, PASP, 104, 533
Harris, K. A., Williger, G. M., Haberzettl, L., et al. 2013, MNRAS, 435, 3125
Hewett, P. C., Foltz, C. B., & Chaffee, F. H. 1995, AJ, 109, 1498
Hinton, S., 2016 MARZ: Redshifting Program, Astrophysics Source Code Library,, ascl:1605.001
Hinton, S. R., Davis, T. M., Lidman, C., Glazebrook, K., & Lewis, G. F. 2016, A&C, 15, 61
Huo, Z.-Y., Fu, Y., Huang, Y., et al. 2025, ApJS, 278, 6
Im, M., Lee, I., Cho, Y., et al. 2007, ApJ, 664, 64
Kim, D., Im, M., Kim, M., et al. 2023, ApJ, 954, 156
Kim, D., Im, M., Lim, G., & Kim, Y. 2024a, JKAS, 57, 95
Kim, D., Kim, Y., Im, M., et al. 2024b, A&A, 690, A283
Kim, T., Sohn, J., & Hwang, H. S. 2025, AJ, 170, 9
Kim, Y., Kim, M., Im, M., et al. 2024c, ApJS, 275, 46
Klemola, A. R., Hanson, R. B., & Jones, B. F. 1994, yCat, 1200, I/200
Laor, A., & Davis, S. W. 2011, MNRAS, 417, 681
Lee, I., Im, M., Kim, M., et al. 2008, ApJS, 175, 116
Li, Z., McGreer, I. D., Wu, X.-B., Fan, X., & Yang, Q. 2018, ApJ, 861, 6
Lindegren, L., Hernández, J., Bombrun, A., et al. 2018, A&A, 616, A2
Lyke, B. W., Higley, A. N., McLane, J. N., et al. 2020, ApJS, 250, 8
Mainzer, A., Bauer, J., Cutri, R. M., et al. 2014, ApJ, 792, 30
Marocco, F., Eisenhardt, P. R. M., Fowler, J. W., et al. 2021, ApJS, 253, 8
Masci, F. J., Laher, R. R., Rusholme, B., et al. 2019, PASP, 131, 018003
McCully, C., Crawford, S., Gabor, K., et al. 2018, astropy/astroscrappy: v1.0.5 Zenodo Release, Zenodo, doi:10.5281/ZENODO.1482019
Nakoneczny, S. J., Graham, M. J., Stern, D., et al. 2025, arXiv:2502.13054
Onken, C. A., Wolf, C., Bian, F., et al. 2022, MNRAS, 511, 572
Onken, C. A., Wolf, C., Hon, W. J., et al. 2023, PASA, 40, e010
Richards, G. T., Myers, A. D., Peters, C. M., et al. 2015, ApJS, 219, 39
Riello, M., D. Angeli, F., Evans, D. W., et al. 2021, A&A, 649, A3
Rizzo, M. L., & Székely, G. J. 2016, WIREs Comput. Stat., 8, 27
Runnoe, J. C., Brotherton, M. S., & Shang, Z. 2012a, MNRAS, 427, 1800
Runnoe, J. C., Brotherton, M. S., & Shang, Z. 2012b, MNRAS, 422, 478
Schlegel, D. J., Finkbeiner, D. P., & Davis, M. 1998, ApJ, 500, 525
Schmidt, M., & Green, R. F. 1983, ApJ, 269, 352
Schneider, D. P., Hall, P. B., Richards, G. T., et al. 2005, AJ, 130, 367
Secrest, N. J., Dudik, R. P., Dorland, B. N., et al. 2015, ApJS, 221, 12
Shen, Y., Hall, P. B., Horne, K., et al. 2019, ApJS, 241, 34
Storey-Fisher, K., Hogg, D. W., Rix, H.-W., et al. 2024, ApJ, 964, 69
Sánchez-Sáez, P., Lira, P., Mejía-Restrepo, J., et al. 2018, ApJ, 864, 87

Tody, D. 1986, Proc. SPIE, 627, 733
Tody, D. 1993, in ASP Conf. Ser. 52, Astronomical Data Analysis Software and Systems II, ed. R. J. Hanisch, R. J. V. Brissenden, & J. Barnes (San Francisco, CA: ASP), 173
Trump, J. R., Hall, P. B., Reichard, T. A., et al. 2006, ApJS, 165, 1
van Dokkum, P. G. 2001, PASP, 113, 1420
Villforth, C., Herbst, H., Hamann, F., et al. 2019, MNRAS, 483, 2441
Wang, C.-J., Bai, J.-M., Fan, Y.-F., et al. 2019, RAA, 19, 149
Werk, J., Tchernyshyov, K., Bish, H., et al. 2024, ApJS, 273, 21
Wolf, C., Lai, S., Onken, C. A., et al. 2024, NatAs, 8, 520
Wright, E. L., Eisenhardt, P. R. M., Mainzer, A. K., et al. 2010, AJ, 140, 1868
Yang, J., Fan, X., Gupta, A., et al. 2023, ApJS, 269, 27
Zhao, Y., Fan, Z., Ren, J., et al. 2018, RAA, 18, 110